Three-dimensional flow structure in an axisymmetric separated/reattaching supersonic flow

Branden M. Kirchner,* Gregory S. Elliott,† and J. Craig Dutton‡

Department of Aerospace Engineering, University of Illinois at Urbana-Champaign, Urbana, Illinois 61801, USA

(Received 26 October 2020; accepted 21 January 2021; published 11 February 2021)

The three-dimensionality of turbulent motions in a massively separated Mach 2.49 longitudinal cylinder wake is investigated using tomographic particle image velocimetry (TPIV). Measurements were acquired within six volumetric subregions of the flow, including the separated shear layer, the recirculation region, the shear layer reattachment region, and the trailing wake, with a large ensemble of measurement volumes (between 2100 and 3300) acquired and processed per region to allow for adequate statistical convergence in the various analyses used. Large streamwise-elongated turbulent structures with a quasiaxial orientation were commonly observed to exist in regions of the flow encountering the adverse pressure gradient associated with shear layer reattachment. The statistical geometry and orientation of these structures within this region of the flow are demonstrated using linear stochastic estimation. The snapshot proper orthogonal decomposition method was also used to decompose the TPIV data into mode shapes. Both an energy-based and an enstrophy-based decomposition were performed, as the three-dimensional TPIV data allow for calculation of all components of the vorticity vector. It is demonstrated that the highest energy-containing modes for many of the TPIV subregions are associated with coherent turbulent structures, such as hairpin vortices or the aforementioned quasiaxial structures. The highest energy-containing mode from the recirculation region data represented 30% of the turbulent kinetic energy within a single mode, and appears to indicate a large-scale global flow interaction between the recirculation region and the separated shear layer with a helical orientation. This large-scale behavior appears consistent with past computational simulations of this flow that also predicted that low-order azimuthal and helical instability modes within the recirculation region play a significant role in the generation of large-scale structures and the production of pressure drag.

DOI: 10.1103/PhysRevFluids.6.024604

I. INTRODUCTION

The turbulence structure of massively separated supersonic flows has long been a strong topic of research interest. Studies of these flows have motivations rooted in both fundamental academic knowledge and practical engineering applications. From an academic perspective, separated/reattaching supersonic flows exhibit a complex flow environment, where the turbulence field is strongly influenced by high levels of compressibility in the shear layer and by extra rates of strain acting both near boundary layer separation and shear layer reattachment [1,2]. This drives nonlinear coupled mechanisms in the turbulence field that are difficult to study and understand. From

*kirchnr2@gmail.com
†elliottg@illinois.edu
‡jcdutton@illinois.edu

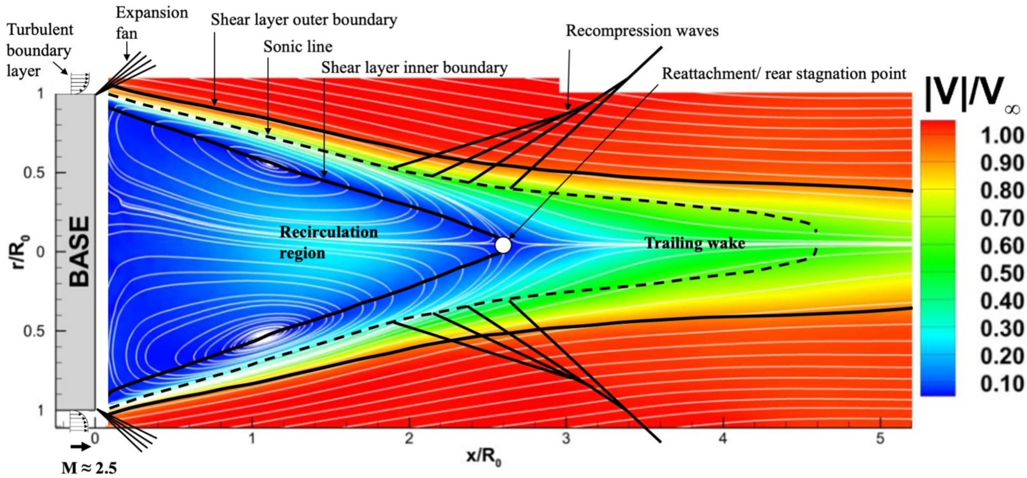

FIG. 1. Data-derived schematic of the time-averaged near-wake flow field using SPIV data originally presented in Ref. [4].

a practical engineering perspective, separated supersonic flows can have a significant influence on vehicle design and efficiency. Mixing characteristics of the shear layer can drive performance in high-speed engine applications, and pressure drag contributions can be quite large in blunt-body vehicle geometries. For example, using in-flight pressure measurements on blunt-based artillery-fired projectiles, Rollstin [3] demonstrated that the pressure drag (i.e., the so-called base drag) constitutes approximately 40% of the total vehicle drag in supersonic flight. Having a more thorough knowledge of the detailed turbulence structure within these types of flows will further the general understanding of how turbulence develops under complex conditions, and will provide essential knowledge in the design of more efficient high-speed vehicle applications.

The current work encompasses an experimental study of the near-wake three-dimensional (3D) turbulence structure behind a blunt-based cylinder aligned at zero angle of attack with a Mach 2.49 freestream (i.e., an axisymmetric base flow). In this type of flow, a turbulent boundary layer separates at the cylinder base, and is rapidly expanded to form the upstream boundary condition for a spatially developing, conical, separated shear layer. This shear layer is bounded above by the supersonic freestream flow, and below by the subsonic recirculating flow. This conical shear layer grows and eventually converges upon itself along the central cylinder axis, where it stagnates and reattaches. Information about this reattachment process propagates upstream along the subsonic separated portions of the flow and induces a streamwise-elongated region of flow field recompression (i.e., an adverse pressure gradient, or APG) that acts to gradually turn the flow radially outward to realign with the central axis. In the supersonic regions of the flow, this APG manifests itself in the form of discrete weak compression waves that coalesce into an oblique shock wave far out in the freestream. Downstream of the reattachment point, the flow transitions into a trailing wake, and rapidly recovers the central velocity deficit to become fully supersonic. A data-derived schematic of the time-averaged features of the current flow is shown in Fig. 1 using stereoscopic particle image velocimetry (SPIV) data that have been previously presented by the current authors [4].

Experimental studies of the near-wake turbulence structure in this flow field date back several decades [5], with the most substantial work coming from a detailed set of laser Doppler velocimetry experiments performed by Herrin and Dutton [2,6–8] in the 1990s. These studies provided the first statistical characterization of the full near-wake turbulence field for this flow, and demonstrated a consistent statistical organization of high-energy large-scale structures within the separated shear layer. However, these experiments only acquired point-by-point two-component velocity measurements and, thus, provided no information about the instantaneous topology of these large-scale structures, which are expected to be highly 3D in nature at the high compressibility levels present [9]. Planar Mie scattering experiments provided two-dimensional (2D) visualizations of these large-scale structures, and demonstrated their high prevalence in the vicinity of shear layer reattachment [10–12]. However, these studies were primarily qualitative in nature, and the ethanol droplets used in these experiments vaporized at the locally high static temperatures in the lower-speed regions of the flow. Thus, these experiments only provided visualizations of the turbulence in the supersonic flow regions, and provided no information about the turbulence structure in the subsonic regions.

Computational simulations of this type of flow also date back several decades. Early on, multiple Reynolds-averaged Navier-Stokes (RANS)-based models were employed, but these have been found to be generally inadequate at predicting key mean flow features, such as the base pressure distribution [13–15]. Multiple direct numerical simulation (DNS) studies have also been performed, but extremely fine grid requirements driving high computational expense generally limit these models to significantly lower Reynolds numbers than in applications or experiments. In particular, the DNS works of Sandberg and Fasel [16–18] were intended to simulate the conditions experienced in the experimental work of Herrin and Dutton [7], but were limited to a freestream Reynolds number that was a factor of approximately 33 lower than those experiments. Large eddy simulation (LES) or detached eddy simulation (DES) models appear to be a more preferred method to simulate this flow, as they provide a more appropriate balance between grid resolution requirements and computational expense [1,19–23]. Although several of these studies are quite accurate in their predictions of mean flow features compared to experiments, these models still have difficulty in accurately predicting the detailed turbulence structure, particularly the Reynolds stresses and other higher-order turbulence statistics. One significant advantage that computational simulations do have over experimental studies of this flow, however, is the availability of time-resolved information. Time-resolved experimental studies of supersonic flows are inherently difficult and expensive due to the short characteristic time scales of the flow, requiring data acquisition recording frequencies on the order of tens to hundreds of kilohertz. To date, only a handful of studies have been able to perform time-resolved experiments of this flow, including high-speed base pressure measurements [24,25], and high-frame-rate Mie scattering images [11].

Several recent works by the current authors have sought to provide a more thorough experimental characterization of the detailed statistical 3D turbulence structure in this specific flow field [4,26,27]. Specific highlights from these works include the identification and statistical characterization of coherent hairpin vortices, as well as demonstrating a qualitative link between the presence of these coherent structures and the mass entrainment characteristics of the separated shear layer. The current paper aims to build on this recent work through the identification and characterization of additional coherent turbulent processes in this complicated flow field utilizing tomographic particle image velocimetry (TPIV), which measures all three components of velocity throughout a volumetric measurement region [28].

The remainder of this paper is organized as follows. Section II outlines the methodologies used in this experimental work, including details about the wind tunnel facility and the TPIV experiments. Section III presents the instantaneous 3D turbulence structure. Section IV discusses statistical trends of the 3D turbulence. Section V presents a modal analysis of the data using proper orthogonal decomposition, and finally, conclusions are given in Sec. VI.

II. METHODOLOGIES

A. Wind tunnel facility

The experiments for this work were performed in the axisymmetric base flow wind tunnel, located within the Gas Dynamics Laboratory at the University of Illinois at Urbana-Champaign. This facility is a blowdown type, and is driven by a 224-kW Ingersoll Rand electric air compressor, which charges an external storage volume of 132 m^3 to a maximum pressure of approximately

1.03 MPa. While charging, the compressed air is filtered and dried to a nominal dew point of 223 K. These conditions allow for continuous steady-state operation of the wind tunnel for up to 3 min, with only approximately 15 min of recharge time between runs.

The high-pressure air flow from the supply reservoir is throttled using a gate valve, and is directed into the stagnation chamber through an angled pipe. This impinges the air flow onto the rear flange of the chamber and promotes stagnation conditions and mixing of the injected TPIV seed particles, which were dispersed into the flow upstream of the stagnation chamber. The air is then forced through a turbulence-reducing screen and honeycomb structure before entering the annular converging-diverging nozzle, which accelerates the flow to a nominal design freestream Mach number of 2.5, with a 145-mm nozzle exit diameter. The annular nozzle exhausts into the center of a rectangular test section, which has four large optical windows (one on each side), and each window has an effective viewing area of $235 \times 209.5\ \mathrm{mm}^2$.

The cylinder model used to induce flow separation is a constant-diameter hollow steel cylinder with a threaded brass cap on the end, and has a constant radius of $R_0 = 31.75$ mm. The brass cap serves as the afterbody from which the flow separates, and is outfitted with static pressure ports along both the afterbody surface and the cylinder base. The weight of this model is fully supported upstream of the screen and honeycomb structure to allow for a nominally axisymmetric boundary layer profile to form along the cylinder. Previously acquired particle image velocimetry (PIV) data in this facility at the nozzle exit have demonstrated a 99% boundary layer thickness on the cylinder of 3.53 mm near the point of separation, a freestream velocity of $V_\infty = 565$ m/s, a freestream Mach number of $M_\infty = 2.49$, and freestream turbulence intensities of $0.008V_\infty$ and $0.004V_\infty$ in the axial and radial directions, respectively. Additionally, during wind tunnel steady-state operation for the experiments of the current work, the stagnation pressure was 409 kPa, the average stagnation temperature was 287 K (the stagnation temperature decreases slightly over the course of a single run of the wind tunnel), and the unit freestream Reynolds number (i.e., $\mathrm{Re} = \rho V_\infty/\mu$) was $44 \times 10^6\ \mathrm{m}^{-1}$. Further details about this facility, including a 3D computer-aided design (CAD) model and operation procedures, are given in Ref. [4].

B. Tomographic PIV experiments

Flow field measurements were acquired in this study using TPIV. These experiments were performed with a set of four LaVision Imager sCMOS cameras, which each have a sensor resolution of 2560×2160 pixels, and a physical pixel size of 6.5 μm. For all cameras, a sharp focus of imaged particles throughout the entire volumetric measurement region was achieved by satisfying the Scheimpflug condition in 3D space (i.e., the imaged object plane, the camera sensor plane, and the lens plane must all intersect along a single line). It was empirically found that a lens $f/11$ was sufficient for all cameras to achieve this sharp focus of particles throughout the entire depth of the measurement volume.

Particle seeding was provided by a ViCount 1300 aerosol generator, which provides a tunable high-volume supply of mineral-oil-based seed particles with a nominal diameter of 200–300 nm. These particle sizes are reported by the manufacturer and have been confirmed via in-house experiments using the measured particle drag response across an oblique shock wave. Using the measured mean shear layer thickness near the separation point as the characteristic length scale, the maximum flow field Stokes number (i.e., the ratio of particle response times to flow response times) was found to be 0.03, with this number decreasing with further streamwise distance from the separation point, as the local characteristic length scales increase. Samimy and Lele [29] demonstrated that tracer particles with a Stokes number of less than 0.05 provide highly accurate tracking of turbulent flow dynamics, indicating that particle lag errors were small in the current experiments.

The seed particles were injected upstream of the stagnation chamber with a high-pressure supply of ultrahigh-purity nitrogen, and are uniformly mixed with the air supply prior to entering the nozzle. Given how these particles were mixed with the air supply, the local particle seed density within the test section closely follows the relative local fluid density (i.e., the seed density is highest

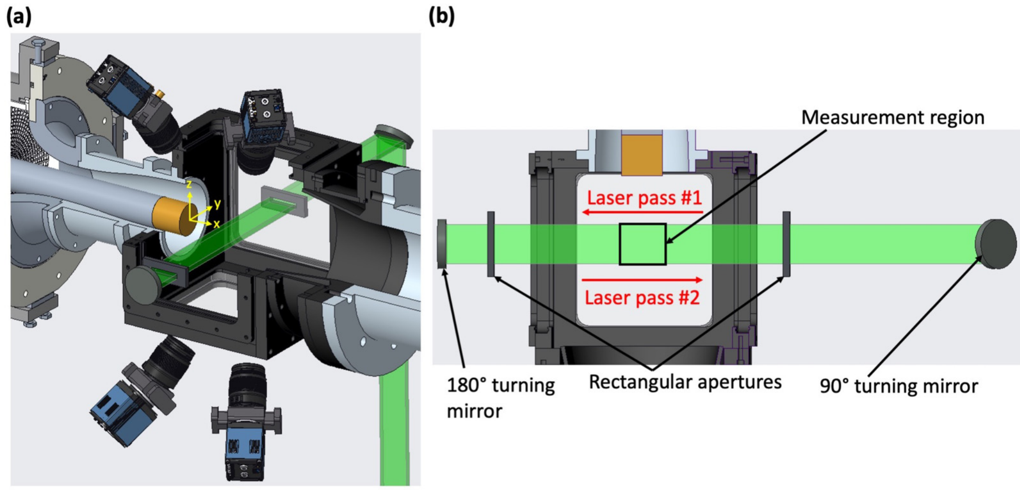

FIG. 2. (a) 3D view CAD model schematic of the TPIV experiments in the base flow wind tunnel and (b) top-down view schematic of the double-pass illumination system.

in the freestream regions, and lowest in the separated recirculating region). Therefore, the rate of output of the seeder was tuned to produce a desired seed density in the region of the flow being measured during any given experiment. "Ghost" particle intensities are a common source of measurement error in TPIV experiments [30], and are a result of seed densities being too high for a given camera configuration. Past literature has demonstrated that seed densities of around 0.05 particles/pixel produce high-quality tomographic reconstructions when using the multiplicative algebraic reconstruction technique (MART) algorithm with a four-camera configuration [28,31]. The measured seed densities in the current experiments were typically found to be in the range of 0.04 to 0.06 particles/pixel, which indicates that ghost particles did not have a significant influence on reconstruction quality in these experiments.

Illumination of the seed particles was achieved using a double-pulsed New Wave Research SOLO Nd:YAG laser, with a maximum pulse energy of approximately 175 mJ/pulse. All digital signals were synchronized for these experiments using a LaVision Programmable Timing Unit (PTU X). To maximize signal strength, all four cameras were arranged in a forward-scatter orientation with respect to the direction of laser propagation. Additionally, a double-pass illumination system was implemented to further increase the signal strength, similar to the experiments of Scarano and Poelma [32] and Schröder *et al.* [33]. To achieve this, a planar mirror was placed on the far side of the test section, and the laser volume was reflected 180° and directed back through the measurement volume a second time. To control the laser divergence, rectangular trimming apertures of equal size were placed on both sides of the test section. The implementation of this double-pass system was found to provide an average increase in recorded signal strength of 12% compared to a single-pass illumination system. This relatively low improvement in signal strength is a result of the reflected laser pass having a backscattering orientation relative to the cameras. A CAD model schematic of a typical TPIV experiment in the base flow wind tunnel is shown in Fig. 2(a), with a top-down view schematic of the double-pass illumination system shown in Fig. 2(b). Additionally, all measurements were acquired in these experiments at a constant rate of 15 Hz, which is several orders of magnitude slower than any known characteristic time scales of this flow [24], so the individual measurement volumes that were acquired are all uncorrelated in time.

All processing of particle images for these experiments was performed in the LaVision DAVIS 10.0 software. Particle images were filtered to reduce measurement noise prior to tomographic reconstruction. A "subtract sliding minimum" filter over a 3×3 pixel window brought the back-

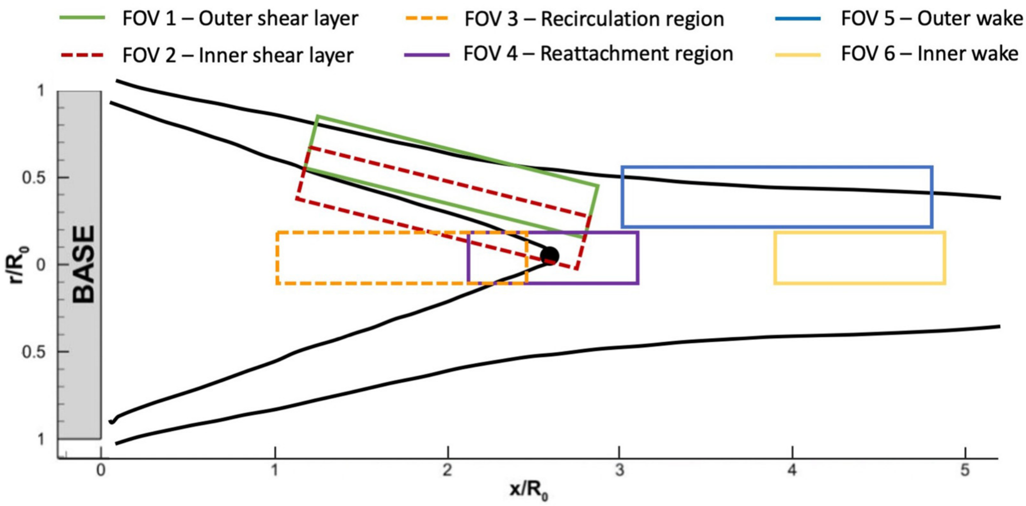

FIG. 3. Schematic showing the locations of all six TPIV measurement volumes intersecting the spanwise symmetry plane. The solid black contours depict the mean shear layer boundaries.

ground intensity down to a near-zero value, a "normalize with local average" filter over a 250 × 250 pixel window removed uneven lighting distributions, and a constant pixel intensity value was then subtracted to floor the background intensity. Image calibration was performed using a single image per camera of a LaVision type 11 two-level calibration target, which has a displacement of 2 mm between calibration planes. The 3D calibration was extrapolated over the entire volumetric measurement domain using a third-order polynomial function. A volumetric self-calibration was then used to refine the calibration accuracy [34]. For all TPIV experiments, disparity vectors were computed on a 9 × 9 × 5 grid within the measurement region, and the self-calibration procedure was iterated until the final average disparity vector length over the entire grid was less than 0.03 pixel. Data from each individual run of the wind tunnel were calibrated separately to mitigate errors associated with equipment misalignment occurring between the separate runs.

Volumetric reconstruction was performed using the MART algorithm with seven iterations. PIV cross-correlation windows were spherical in shape and utilized a Gaussian weighting function, with 75% spatial overlap occurring between successive passes. For each set of experiments, four different iterative window sizes were used. The earlier passes utilized large windows, 160 voxels in diameter, and implemented voxel binning to search for cross-correlation peaks in a computationally efficient manner. In successive passes, the window diameter and the amount of binning were reduced. The final window size was empirically determined for each set of experiments, depending on the local measured seed density, and utilized three adaptive-geometry passes with no voxel binning. Typically, the final cross-correlation windows contained between five and ten tracer particles. Finally, the velocity vector fields produced by this procedure were filtered for statistical outliers using a "universal outlier detection" method, which removed spurious vectors in a local 5 × 5 × 5 vector neighborhood. Typically, this filter removed less than 1% of the total velocity vectors from a given measurement volume.

In the current work, six different volumetric subregions within the flow field were measured using TPIV. Within each region, a large ensemble of measurement volumes (between 2100 and 3300) were acquired and processed to allow for adequate convergence in the various turbulence analyses used. The locations of each of these six volumetric regions within the flow field are shown in Fig. 3, where the black contour lines in this figure depict the same mean flow shear layer boundaries as in Fig. 1. Also note that Fig. 3 depicts the intersection of these measurement volumes with the spanwise flow symmetry plane (i.e., a plane coincident with the central axis), and the actual volumes extend

TABLE I. TPIV experimental parameters.

	FOV 1	FOV 2	FOV 3	FOV 4	FOV 5	FOV 6
Final window diameter (voxels)	56	64	64	64	56	56
Image cale (pixel/mm)	40.6	41.2	46.7	42.6	37.1	46.5
Number of volumes acquired	2687	2409	2525	3283	2451	2169
Volume length (mm)	52.4	53.2	46.2	33.4	57.5	27.4
Volume width (mm)	36.1	41.9	41.0	40.9	30.5	38.9
Volume thickness (mm)	9.4	9.8	9.3	9.1	11.4	9.4
Vector spacing (mm)	0.347	0.391	0.345	0.379	0.381	0.304
Number of vectors along length	152	137	135	89	152	91
Number of vectors along width	105	108	120	109	81	129
Number of vectors along thickness	28	26	28	25	31	32

symmetrically into and out of the page. The acronym “FOV” in Fig. 3 denotes “field of view” and establishes a labeling system for each of the six regions that will be utilized throughout the remainder of this paper. Furthermore, various details about these six different data sets are given in Table I, including physical measurement volume dimensions, measurement ensemble sizes, and the number of three-component velocity vectors along each dimension of the rectangular volumes. Further details regarding validation metrics for these TPIV data can be found in Ref. [26].

III. INSTANTANEOUS TURBULENCE STRUCTURE

In this section, the volumetric instantaneous flow is examined. Visualizations of 3D velocity surfaces can provide useful information about turbulent motions, but visualizations of the 3D geometry of the turbulent structures themselves, using quantities other than a velocity component, are typically far more interesting. Throughout this paper, the geometry of turbulent structures is educed using the swirling strength criterion (λ_{ci}), which is a commonly used metric to visualize turbulent structures in 3D computational fluid dynamics data. In a fluid region exhibiting rotational motion, computing the eigenvalues of the local velocity gradient tensor will produce one real-valued eigenvalue and a complex conjugate pair. The swirling strength criterion is then defined as the magnitude of the imaginary component of that complex conjugate eigenvalue pair, which Zhou *et al.* [35] present as being proportional to the strength of local rotational motions. Additionally, Kolar [36] demonstrated that the λ_{ci} criterion was one of the few vortex identification methodologies that could be accurately applied towards the study of compressible turbulence. Previous work by the authors [27] has demonstrated the convective Mach number in the shear layer of this flow (i.e., the local Mach number in the relative frame of reference of the large-scale structures [37]) to range between 1.02 and 1.38, which indicates very high levels of compressibility. Von Terzi *et al.* [38] examined the use of different structure identification schemes in a DNS of this same flow. They found that different structure identification criteria highlighted different large-scale structure types within a given instantaneous snapshot of the flow, particularly in the far upstream portions of the separated shear layer. However, the current authors have investigated the use of both the λ_{ci} criterion and the Q criterion (defined as the second invariant of the velocity gradient tensor) as metrics to educe coherent structures in this flow, and have observed no significant qualitative differences in identified large-scale structures between the two methodologies in the more downstream regions investigated herein.

Figure 4 demonstrates a typical instantaneous measurement volume from the FOV 1 region, which was located in the higher-speed portions of the separated shear layer along an angled orientation. Throughout this paper, velocity components are presented in a cylindrical coordinate system (i.e., V_r, V_θ, and V_x for radial, azimuthal, and axial velocity components, respectively), with a Cartesian spatial coordinate system defined by the set of axes shown in Fig. 2(a). Figure 4(a) shows

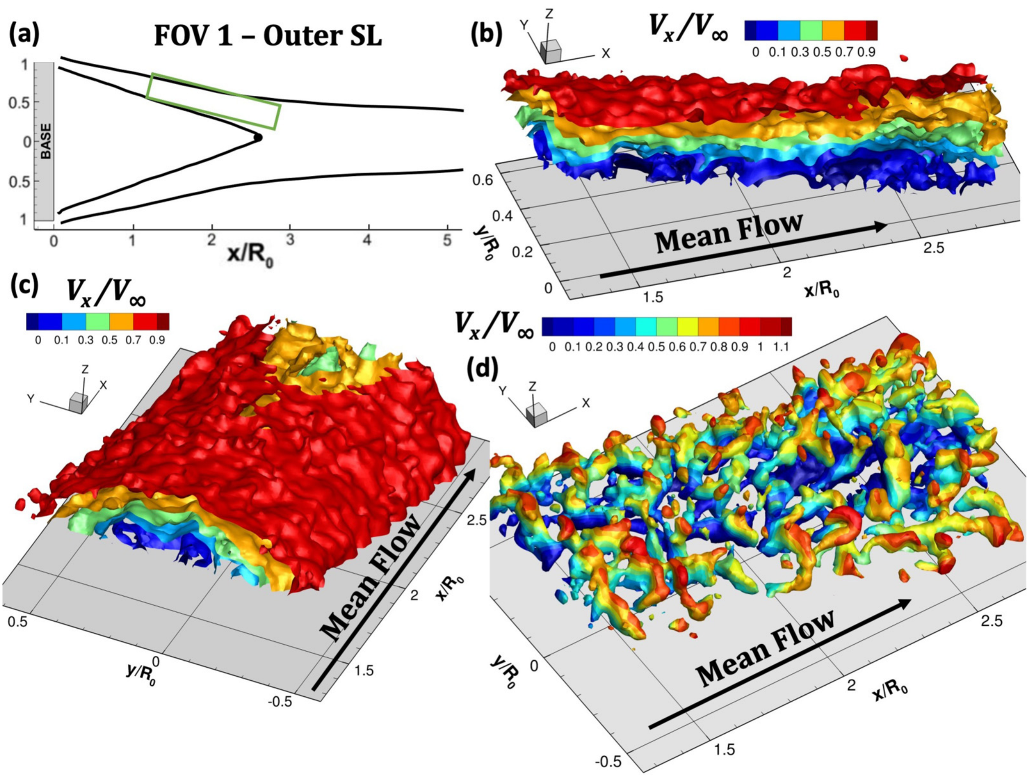

FIG. 4. Example instantaneous TPIV measurement volume from FOV 1. (a) Location of FOV 1 within the flow, (b) subregion of velocity contours for $y/R_0 > 0$, (c) full field-of-view velocity contours, and (d) turbulent structures within the measurement volume, educed by $\lambda_{\mathrm{ci}} = 2$. The coloring of contours for (b–d) is defined by V_x/V_∞.

the location of the measurement volume relative to the mean flow features, Figs. 4(b) and 4(c) show instantaneous V_x/V_∞ isocontours, and Fig. 4(d) shows the instantaneous turbulent structures present within this measurement volume. In Fig. 4(d), the geometry of the structures is educed by λ_{ci}, but the coloring is defined by V_x/V_∞, which highlights the instantaneous velocity gradients present across the structures.

Figure 4(c) shows the full volumetric extent of the instantaneous V_x/V_∞ isocontours, but due to the conical nature of this flow, the lower-speed contours tend to nest within the boundaries of the higher-speed contours, which makes visualization difficult. To circumvent this, one-half of the data in Fig. 4(c) was masked across the $y/R_0 = 0$ plane, and the sliced velocity region is shown in Fig. 4(b). The highly 3D instantaneous nature of the shear layer can be observed from the velocity contours in Fig. 4, with many convolutions of varying size and geometry present. In the downstream portions of the measurement volume, the highest-speed contour (i.e., the red contour) is cut off along the edges of the volume, which is a result of the APG in this region turning the flow radially outward, and beyond the range of the measurement region. Additionally, it can be observed that a relatively large azimuthal extent of the 3D flow is obtained within a single measurement volume.

Many of the turbulent structures educed in Fig. 4(d) are fairly large scale, and seem to be most heavily concentrated in the downstream portions of the measurement volume, where the APG acts as an additional source of vorticity production. Additionally, several coherent structure geometries can be observed in Fig. 4(d), such as hairpin-shaped vortices, which were demonstrated to be common features of this flow in previous work by the authors [26], as well as streamwise-elongated turbulent

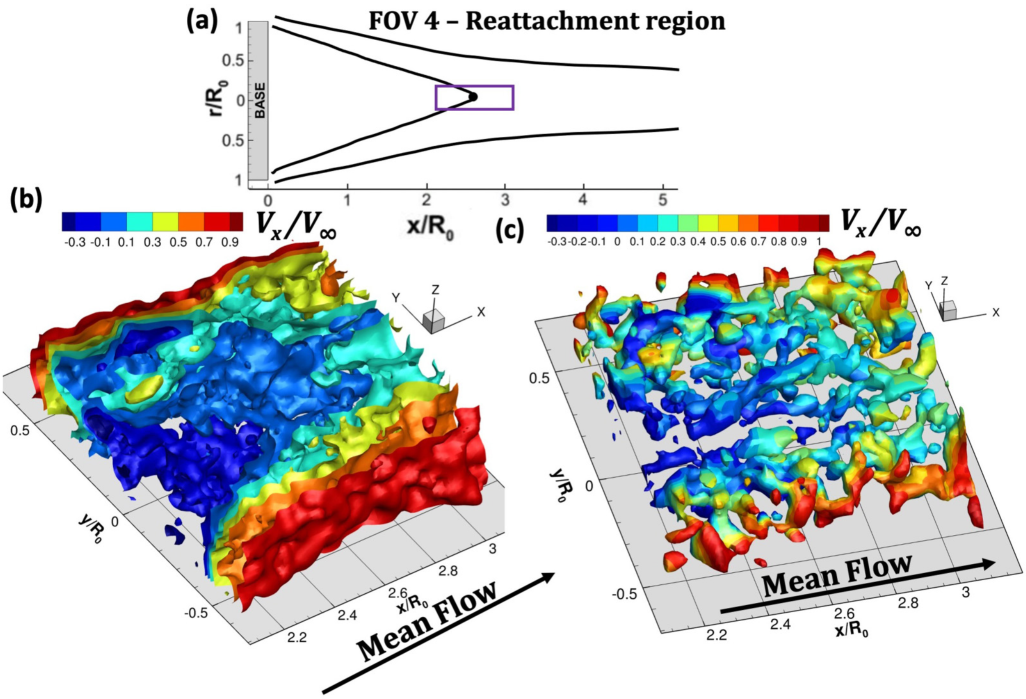

FIG. 5. Example instantaneous TPIV measurement volume from FOV 4. (a) Location of FOV 4 within the flow, (b) full field-of-view velocity contours, and (c) turbulent structures within the measurement volume, educed by $\lambda_{ci} = 2$. The coloring of contours for (b) and (c) is defined by V_x/V_∞.

structures. The largest structures within this measurement volume also appear to exist in the lower-speed portions of the flow (i.e., the blue contours), which is in agreement with previous results, as the subsonic portions of the shear layer have been demonstrated to be the highest turbulent energy regions of this flow [4,7].

Another example volumetric snapshot is shown in Fig. 5, this time from the FOV 4 measurement region, which is centered about the mean shear layer reattachment point. Similar to the previous example, Fig. 5(a) shows the location of the measurement volume relative to the mean flow, Fig. 5(b) shows the instantaneous V_x/V_∞ contours, and Fig. 5(c) displays the turbulent structures educed by λ_{ci}.

The FOV 4 measurement volume shown in Fig. 5 traverses the full spanwise width of this region of the flow and captures the conical shear layer on both sides. The reattachment point is typically dictated by the $V_x/V_\infty = 0$ contour, which Fig. 5(b) demonstrates is highly convoluted instantaneously. This measurement region also displays many large-scale turbulent structures throughout the entire measurement volume, both in the high-speed and low-speed flow regions. Similar to Fig 4(d), several arch-shaped and streamwise-elongated structures can be observed in Fig 5(c), demonstrating significant levels of coherent turbulent activity in the vicinity of the reattachment point.

Examination of instantaneous velocity fields in the high-speed trailing wake region (FOV 5) commonly revealed a very large-scale turbulent behavior, wherein the lower-speed portions of the measurement volumes would typically branch off from one another and split into multiple distinct flow segments. When these lower-speed segments branch apart, the void in between them is filled with a region of relatively higher-speed fluid. Two instantaneous examples of this behavior are shown in Fig. 6, where the flow in the first example [Figs. 6(a) and 6(b)] branches into two distinct segments, and the flow in the second example [Figs. 6(c) and 6(d)] branches into three segments.

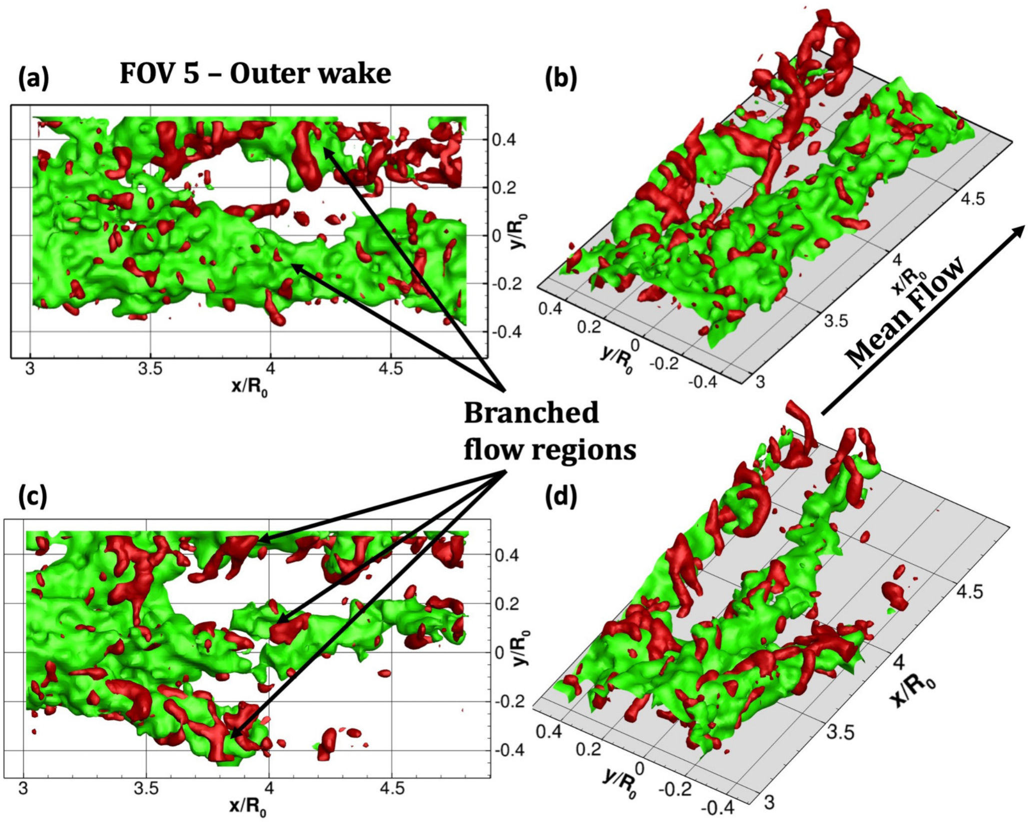

FIG. 6. Two example instantaneous TPIV measurement volumes from FOV 5. Green isosurfaces depict $V_x/V_\infty = 0.65$ and red isosurfaces depict $\lambda_{ci} = 2.25$. (a) Top-down view of example 1, (b) 3D view of example 1, (c) top-down view of example 2, and (d) 3D view of example 2.

In both examples shown in Fig. 6, the green isocontours represent $V_x/V_\infty = 0.65$, and the red isocontours represent $\lambda_{ci} = 2.25$, which educes the turbulent structures present in the vicinity of these branched flow segments.

In the first example [Figs. 6(a) and 6(b)], there is a clear branching of the flow into two distinct segments, where the white region in between them is filled with higher-speed fluid than the $V_x/V_\infty = 0.65$ contours. The conical nesting of velocity contours makes simultaneous visualizations of both the high- and low-speed flow segments difficult. One of the branched segments in this example appears to be enveloped by many large-scale vortical structures (in red), while the other branch displays only a few smaller-scale structures. This was a commonly observed behavior across many of these instantaneous snapshots, wherein the flow branch nearest to the central axis would behave more similarly to the mean flow, with little large-scale turbulent activity, and the further outward branches exhibited a higher prevalence of large-scale structures. The second example snapshot [Figs. 6(c) and 6(d)], which displays a branching of the flow into three segments, also displays this behavior, where the central branch displays very few turbulent structures, and the further outward branches have a higher prevalence of large-scale structures. This behavior constitutes a large-scale coherent turbulent motion, which appears to commonly occur alongside instances of significant vorticity production in the APG region just downstream of shear layer reattachment.

In addition to the arch-shaped hairpin structures in this flow, large-scale streamwise-elongated structures were also commonly observed, primarily in the vicinity of the reattachment point for the

FOV 1, FOV 2, and FOV 4 measurement regions, as well as some similar structures of this type existing further downstream in the FOV 5 region. The authors postulated that these streamwise-elongated structures rotate about their central axis, but the 3D λ_{ci} criterion provides no information about rotational directionality for the structures it educes. Therefore, to confirm that the rotation of this type of structure was about its central axis (which was observed to approximately align with the x coordinate), a 2D directional swirling strength criterion was implemented to identify axially oriented fluid swirl.

The 3D λ_{ci} criterion is defined by the eigenvalues of the full velocity gradient tensor. Similarly, a 2D plane can be constructed within the data, whose outward normal vector aligns with a desired direction. The magnitude of the imaginary component of the complex conjugate eigenvalue pair of the 2D velocity gradient tensor within that plane then identifies rotational motion about that outward normal vector. Furthermore, the direction of rotation for that component (i.e., positive or negative rotation) can be determined by examining the sign of the corresponding component of the vorticity vector. The 2D velocity gradient tensors for each of the three cylindrical coordinate directions are defined by Eqs. (1), and the full definition of the 2D swirling strength criterion (i.e., $\lambda_{ci,k}$, for 2D swirl aligned with the kth coordinate direction) is given by Eqs. (2), where ω_k represents the kth component of the local vorticity vector:

$$J_r = \begin{bmatrix} \frac{1}{r}\frac{\partial V_\theta}{\partial \theta} + \frac{V_r}{r} & \frac{\partial V_\theta}{\partial x} \\ \frac{1}{r}\frac{\partial V_x}{\partial \theta} & \frac{\partial V_x}{\partial x} \end{bmatrix}, \quad J_\theta = \begin{bmatrix} \frac{\partial V_r}{\partial r} & \frac{\partial V_r}{\partial x} \\ \frac{\partial V_x}{\partial r} & \frac{\partial V_x}{\partial x} \end{bmatrix}, \quad J_x = \begin{bmatrix} \frac{\partial V_r}{\partial r} & \frac{1}{r}\frac{\partial V_r}{\partial \theta} - \frac{V_\theta}{r} \\ \frac{\partial V_\theta}{\partial r} & \frac{1}{r}\frac{\partial V_\theta}{\partial \theta} + \frac{V_r}{r} \end{bmatrix}, \tag{1}$$

$$\mathrm{eig}(J_k) = \lambda_{\mathrm{real},k} \pm i\lambda_{\mathrm{ci},k}, \quad \lambda_{\mathrm{ci},k} = \mathrm{sign}(\omega_k)|\lambda_{\mathrm{ci},k}|. \tag{2}$$

Although the axial swirling strength could be defined more simply here in terms of the Cartesian directions and velocity components, it is defined in terms of the cylindrical components in Eqs. (1) for consistency. Additionally, all spatial derivative quantities were computed using the method of Savitsky-Golay filtering [39]. In practice for TPIV data, this technique is performed by fitting a second-order polynomial function in a least-squares sense within a 3D window of velocity field data, and then the coefficients of the fit function provide spatially smoothed approximations of the derivative quantities. Further details about this technique as a method of computing spatial derivatives for TPIV data are given by Elsinga *et al.* [40].

Two separate example measurement volumes from the FOV 1 shear layer data are shown in Fig. 7. In this figure, the full measurement volumes for the two examples are shown in Figs. 7(a) and 7(d), where the green surfaces denote $V_x/V_\infty = 0.2$, and the red surfaces denote $\lambda_{ci} = 2.75$. To the right of each of these measurement volumes is a zoomed-in region, where the upper zoomed-in region for each example [i.e., Figs. 7(b) and 7(e)] depicts the structures as educed by λ_{ci}, and the lower zoomed-in region for each example [i.e., Figs. 7(c) and 7(f)] depicts the same region as Figs. 7(b) and 7(e), but with the structures instead educed by $\lambda_{ci,x}$ (i.e., 2D axial swirl).

In both of the examples shown in Fig. 7, a large structure can be observed in the downstream portion of the measurement volume, within the low-speed fluid region, and near the mean reattachment location. Figures 7(b) and 7(e) show the λ_{ci} contours that educe these structures, but the geometry in each example is highly convoluted and covered with bumps. This highlights an inherent limitation of the λ_{ci} metric, in that it cannot distinguish between nearby turbulent structures (i.e., it blends them together as a seemingly continuous 3D contour). In reality, the bumps observed along this structure are most likely a collection of small-scale turbulent structures existing along the periphery of the core structure. However, when the metric is changed to educe purely axially rotating fluid, using $\lambda_{ci,x}$ [Figs. 7(c) and 7(f)], the geometry of the core structures in both examples becomes much clearer, and many of the bumps disappear. This metric clearly demonstrates that the core structures in these examples exhibit a rotation primarily aligned in the x direction, and that the structures themselves are quite large in size. To provide a meaningful spatial scaling, the lengths of these structures are presented in Figs. 7(c) and 7(f) as a fraction of the local shear layer vorticity thickness [41], δ_ω, which is a common metric used to quantify the transverse thickness of separated shear layers [42]. The vorticity thickness value used to scale either structure was taken as the Reynolds-averaged δ_ω

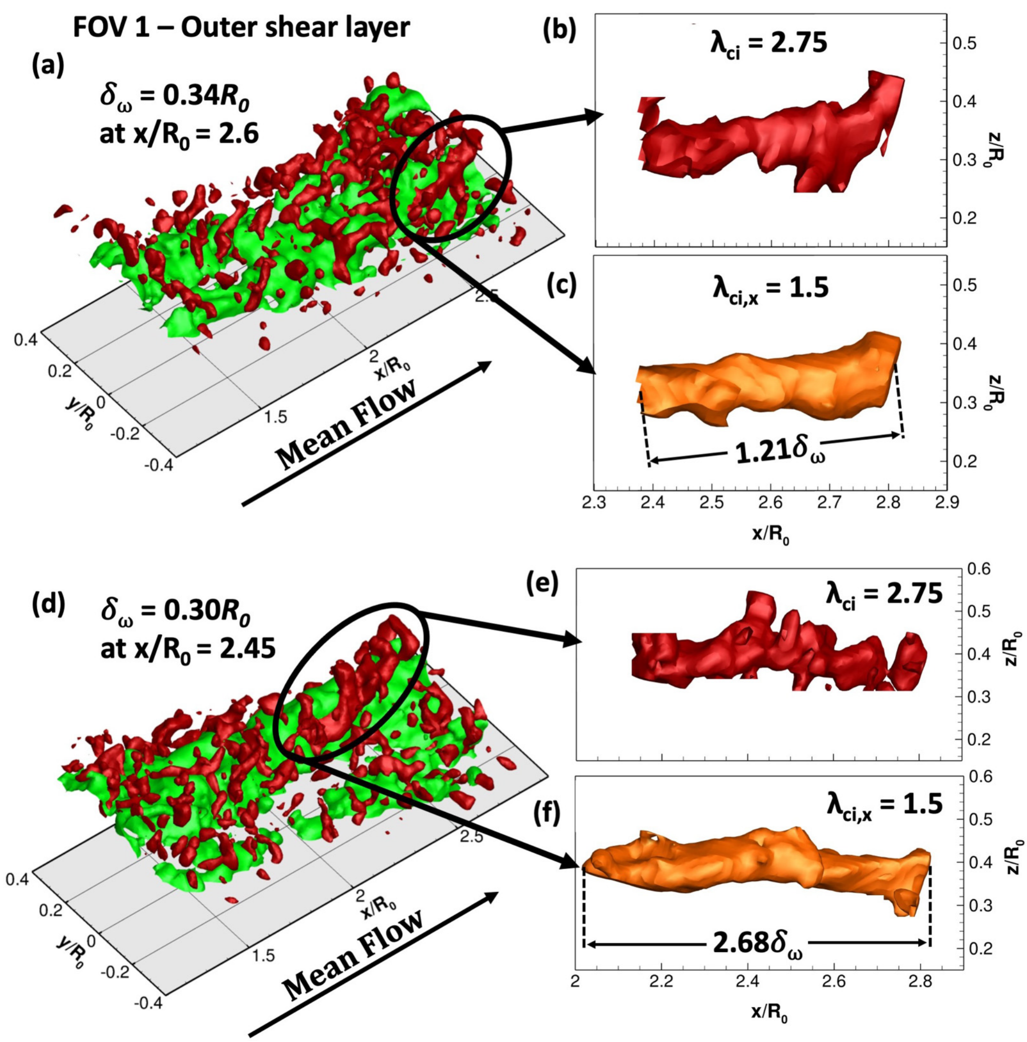

FIG. 7. Two example instantaneous TPIV measurement volumes from FOV 1. Green isosurfaces are defined by $V_x/V_\infty = 0.2$, and red isosurfaces are defined by $\lambda_{ci} = 2.75$. (a) Full-field example 1, (b) zoomed-in structure from (a) with geometry educed by λ_{ci}, (c) same zoomed-in region as (b), but with geometry educed by $\lambda_{ci,x}$, (d) full-field example 2, (e) zoomed-in structure from (d) with geometry educed by λ_{ci}, and (f) same zoomed-in region as (e), but with geometry educed by $\lambda_{ci,x}$.

value at the streamwise-central location of each structure. With this scaling applied, it can be seen in Fig. 7 that these instantaneous structures are indeed very large compared to the global mean flow features, with the first example being just longer than the local vorticity thickness is wide, and the length of the second example being nearly three times the width of the local vorticity thickness. Additionally, both examples shown in Fig. 7 happen to demonstrate positive rotations about the x coordinate, but a large number of instantaneous measurement volumes also demonstrated these types of structures exhibiting negative rotations about the x coordinate. No preferential direction of rotation was observed for these structures within these TPIV data, which is an enforced constraint on the flow by the Reynolds-averaged axial symmetry.

The DESs of this flow by Simon *et al.* [1] predicted the presence of "mushroom-shaped" lobes in the near reattachment region, which qualitatively agreed with the planar Mie scattering experiments of Bourdon and Dutton [10]. These lobes were attributed in these studies to the presence of large-scale streamwise vortices, which they noted were most prominent in the near reattachment region. These previous findings are consistent with the current data, as the instantaneous large-scale streamwise-elongated vortices educed in the TPIV data are typically only observed within the APG regions of the flow near reattachment. Given that these structures are only observed within regions of the flow encountering the APG, it stands to reason to postulate that the APG itself contributes to their generation. A possible mechanism responsible for the generation of these structures could be an unsteady component of the baroclinic torque in this region. High levels of compressibility within the shear layer give rise to significant density gradients (which align transverse to the direction of shear layer convection), and the APG acts approximately along the direction of shear layer convection. This misalignment of the density and pressure gradients produces baroclinicity, which can act as a significant additional source of vorticity production in highly compressible separated/reattaching flows [16]. The baroclinic torque vector, given by $\rho^{-2}(\vec{\nabla}\rho \times \vec{\nabla}P)$, is axisymmetric for the Reynolds-averaged flow, and produces an additional torque on the fluid that aligns with the torque also induced by the mean flow shearing. Instantaneously, however, large-scale geometric convolutions of the pressure and/or density gradients in the θ direction, which are likely common events given the highly convoluted flow field in the vicinity of the reattachment point, as shown in Fig. 5, would produce unsteady components of the baroclinic torque vector that could induce a large-scale roll-up of fluid in the x direction. However, this mechanism can only currently be postulated, as neither pressure nor density field information (mean or instantaneous) is available with the current data.

IV. STATISTICAL TURBULENCE STRUCTURE

A. Mean swirling strength trends

To further examine the directional trends of rotational motion in this flow, all three cylindrical components of the 2D swirling strength [Eqs. (1) and (2)] were computed and averaged across the full ensemble of TPIV snapshots. In a Reynolds-averaged sense, the mean radial and axial components of 2D swirl are analytically zero, as the flow symmetry requires the positively oriented rotations to average out the negatively oriented ones. Therefore, to obtain a measure of average rotational strength, the ensemble average of the magnitude of these 2D swirling strength values was computed. Furthermore, a purely ensemble-based average would be flawed in identifying average spatial trends of rotational strength, as the averaging would exhibit an intermittency bias towards locations that exhibited a higher statistical likelihood of a vortex structure existing at that location during any given instantaneous snapshot. For a local velocity gradient tensor, the eigenvalues will only return a complex conjugate pair if the local fluid state exhibits rotational motion; otherwise the returned eigenvalues are purely real. Therefore, the definition of the swirling strength inherently acts as an intermittency filter in detecting vortical structures, as opposed to the vorticity vector, which will always return a nonzero value, even if the nonzero value is simply a result of shear or measurement noise. If the local eigenvalues are complex for a snapshot at a given location, then a vortex was measured to be passing through that location, and it is included in the average. Otherwise, if the eigenvalues are purely real, then no vortex was measured at that location, and that snapshot is excluded from the local average. The results of this intermittency-filtered ensemble average for the magnitude of 3D swirl, as well as all three 2D cylindrical components along the spanwise symmetry plane (i.e., the $y/R_0 = 0$ plane) for the TPIV FOV 1, FOV 2, and FOV 5 regions, is shown in Fig. 8. In Figs. 8(b)–8(d), the contours for all three 2D components of mean swirl are presented on the same color scale, in order to provide a comparison of rotational strength between the components. Additionally, in this figure, the dashed black contour denotes the mean sonic line, and the solid black contour denotes the low-speed shear layer boundary.

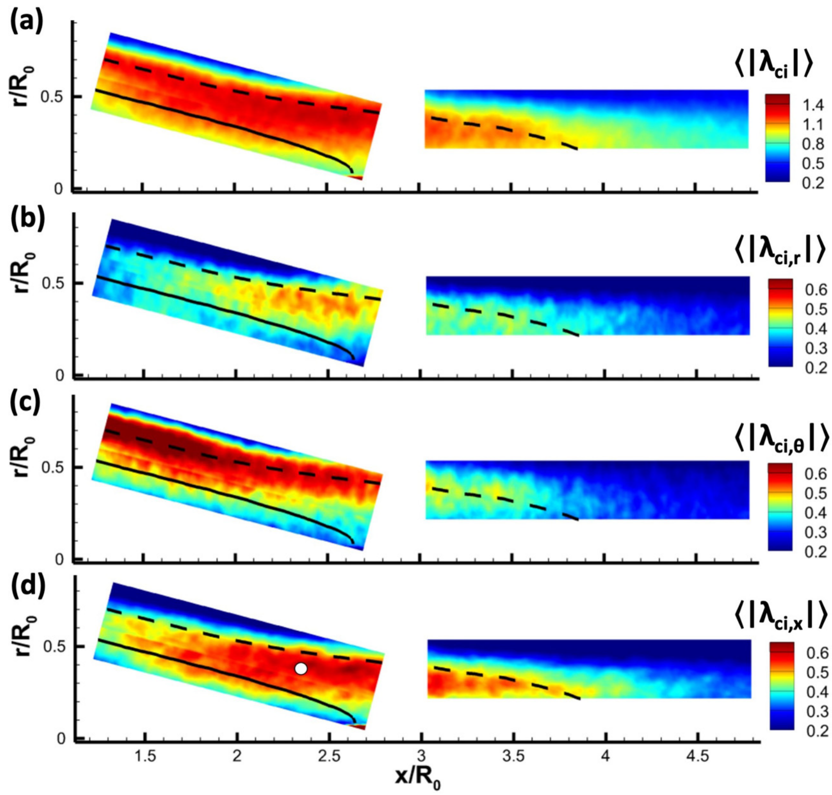

FIG. 8. Intermittency-filtered ensemble-average contours of swirling strength magnitude along the $y/R_0 = 0$ flow symmetry plane. (a) 3D (nondirectional) swirl, (b) 2D radial swirl, (c) 2D azimuthal swirl, and (d) 2D axial swirl. Data for this figure emanate from FOV 1, FOV 2, and FOV 5. The solid black contour is approximately the low-speed shear layer boundary, and the dashed black contour is the mean sonic line. The white dot denotes the reference location for Fig. 9.

In Fig. 8(a), the mean contours of nondirectional 3D swirl demonstrate that the strongest rotational motions in this flow exist throughout the subsonic portions of the shear layer (i.e., bounded between the sonic line and the low-speed shear layer boundary), with the highest-valued contours being just below the sonic line near reattachment. As the flow transitions into the trailing wake, the contours of $\langle|\lambda_{ci}|\rangle$ remain high in magnitude for some streamwise extent, but continually decay with further streamwise progression as the turbulence loses strength and organization further downstream.

The azimuthally rotating turbulent structures, identified by Fig. 8(c), are most prevalent further upstream, approximately centered about the sonic line. This seems reasonable as these rotations are primarily driven by the mean flow shear generating Kelvin-Helmholtz instabilities. As the flow progresses downstream, the shear layer grows spatially and the mean shearing decays, and the strength of the azimuthal structures appears to decay as well. This is particularly evident in the trailing wake region, where downstream of the end of the mean APG region ($x/R_0 \approx 3.7$), the strength of the azimuthally rotating structures diminishes rapidly, as the mean baroclinicity vanishes, and the local mean flow shearing is much lower than further upstream.

The radial and axially rotating structures, however, cannot be produced by mean flow-induced turbulence production, and are thus a result of unsteady 3D instability mechanisms. In the far upstream portions of the shear layer, the mean axial swirl [Fig. 8(d)] is small compared to the azimuthal swirl [Fig. 8(c)]. Throughout the APG region of the shear layer and trailing wake, however, the axial swirl contours are much larger in magnitude, and either match or exceed the strength of the azimuthal swirl contours in the vicinity of reattachment. These $\langle|\lambda_{\mathrm{ci},x}|\rangle$ contours persist quite far into the trailing wake, and it appears that this is actually the dominant component of rotational motion within the trailing wake. Additionally, these structures appear most heavily concentrated in the subsonic portions of the flow, with their influence diminishing rapidly when traversing into the supersonic portions of the flow [i.e., above the dashed black line in Fig. 8(d)].

Furthermore, although comparatively small in magnitude, the $\langle|\lambda_{ci,r}|\rangle$ contours of Fig. 8(b) appear to directly overlap spatially with the $\langle|\lambda_{\mathrm{ci},x}|\rangle$ contours of Fig. 8(d), with the same increases in magnitude occurring in the APG region of the shear layer. This indicates that the same type of structure could be driving the production of both of these components of swirl, wherein the structure exhibits a quasiaxial orientation, such as the example shown in Fig. 7(c), with components of rotation in both the axial and radial directions. Logically, the authors postulate that these significant axial and radial swirl contours in the reattachment region of Fig. 8 are primarily driven by the large-scale quasiaxial structures that were discussed in the previous section of this paper.

B. Linear stochastic estimation

In order to examine the statistically averaged flow structure in the high-$\langle|\lambda_{\mathrm{ci},x}|\rangle$ contour regions of Fig. 8(d), linear stochastic estimation (LSE) is utilized [43]. LSE is a method for approximating the conditional average of turbulent velocity fields given the condition that some turbulent event (E) has occurred at a reference location. It is a preferable technique in experimental work, as it provides an estimate of the conditional average without the need for conditionally sorting an ensemble of data, which can already be limited in size. LSE approximates the conditional average of a fluctuating velocity component (V') by expanding $\langle V'|E\rangle$ in a power series about $E = 0$, retaining only the linear term, and minimizing the mean-squared error between the estimate and the actual conditional average. The resulting equation from this process is given by Eq. (3):

$$V'_{i,c} = \langle V'_i(x, y, z)|E(x_{\mathrm{ref}}, y_{\mathrm{ref}}, z_{\mathrm{ref}})\rangle \approx \frac{\langle V'_i(x, y, z)E(x_{\mathrm{ref}}, y_{\mathrm{ref}}, z_{\mathrm{ref}})\rangle}{\langle E(x_{\mathrm{ref}}, y_{\mathrm{ref}}, z_{\mathrm{ref}})^2\rangle}E. \tag{3}$$

In the LSE analysis, the conditional average of a fluctuating velocity component (denoted $V'_{i,c}$ for the ith component) at some arbitrary (x, y, z) location is computed given that some turbulent event (E) has occurred at a chosen reference location, $(x_{\mathrm{ref}}, y_{\mathrm{ref}}, z_{\mathrm{ref}})$. Ultimately, this method reduces the conditional average to a function of unconditional two-point correlation data between the velocity fluctuations and the chosen turbulent event. The stand-alone E term on the right-hand side of Eq. (3) represents the choice of E (i.e., a chosen, single, scalar quantity), while the E terms that exist inside the brackets represent the measured ensemble of E values within the data at the reference location. Additionally, because this scalar choice of E only acts to linearly scale the conditional velocity field, it is sufficient to choose any arbitrary positive or negative value (i.e., setting $E = +1$ encompasses all positively signed events, and vice versa for $E = -1$) [44].

Using this LSE technique, conditional averages utilizing $E = \lambda_{\mathrm{ci},x}$ would nominally produce the statistically averaged 3D turbulent flow associated with the high-$\langle|\lambda_{\mathrm{ci},x}|\rangle$ contours of Fig. 8. Although it is believed that both the radial and axial swirl values of Fig. 8 are driven by the same type of turbulent structure, the magnitude of axial swirl was clearly dominant over the radial swirl. Therefore, the LSE analysis was performed here utilizing $E = \lambda_{\mathrm{ci},x}$, with the reference point chosen to be in the highest-magnitude $\langle|\lambda_{\mathrm{ci},x}|\rangle$ region. The actual location of the reference point is denoted by the white dot in Fig. 8(d), and this analysis was performed using the TPIV FOV 2 data set. The results of this LSE analysis utilizing $E = \lambda_{\mathrm{ci},x} = +1$ are shown in Fig. 9. In this figure, the structure is educed by $\lambda_{\mathrm{ci},c}$, which is the 3D swirling strength criterion computed on the conditional velocity field, and the vectors indicate the LSE-averaged velocity vectors along the periphery of the educed structure. Additionally, the LSE analysis here was performed solely on the velocity fluctuations, with the influence of the mean flow subtracted beforehand.

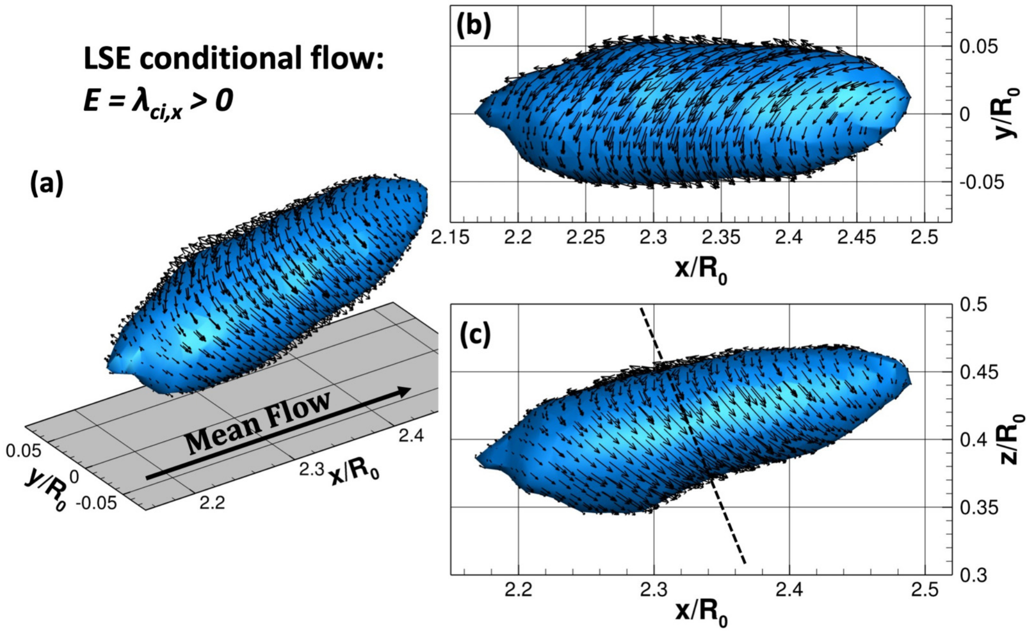

FIG. 9. LSE-resolved quasiaxial structure conditioned on $E = \lambda_{ci,x} > 0$, with geometry educed by $\lambda_{ci,c} = 0.5$. The LSE reference location is denoted by the white dot in Fig. 8(d). Vectors represent the conditional velocity fluctuations along the periphery of the $\lambda_{ci,c}$ isosurface. (a) 3D view of the LSE-resolved structure, (b) top-down view of (a), and (c) side view of (a).

From Fig. 9, it can be seen that the LSE procedure produces an elongated structure with a quasiaxial orientation. The geometry and orientation of this statistical structure are quite similar to the instantaneous structure shown in Fig. 7(c). The vectors around the periphery of the structure in Fig. 9 demonstrate that the conditionally averaged flow rotates about the central axis of this structure, with a slight helical orientation of the rotating flow vectors shown in the top-down view of Fig. 9(b). The rotation of fluid about this quasiaxial orientation is consistent with the mean swirl trends of Fig. 8, which demonstrated a dominant axial component of swirl, along with a smaller but still significant component of radial swirl. Additionally, as the flow symmetry requires the ensemble average of axial rotations to be zero, the LSE average based on the oppositely signed condition of $E = \lambda_{ci,x} = -1$ was also performed. This procedure produced an identical structure to that of Fig. 9, but with the rotation aligned in the opposite direction.

In order to quantify the size and orientation of this statistical structure, Fig. 10 shows contour plots of the $\lambda_{ci,c}$ contours from the structure shown in Fig. 9. Figure 10(a) shows a cross-sectional slice through the structure along the $y/R_0 = 0$ plane, and Fig. 10(b) shows a slice when viewing along the central axis of the structure [i.e., viewing orthogonally to the dashed black line in Fig. 9(c)].

Figure 10 demonstrates that the average quasiaxial structure in this region of the flow is indeed very large scale, with an average length of approximately 1.15 times the local shear layer vorticity thickness, and has an average diameter of $0.37\delta_\omega$. Additionally, the primary axis of this statistical structure is oriented approximately 15° above the horizontal x axis, which is then about 30° relative to the local mean shear layer direction, as the local shear layer fluid convects at a mean orientation of approximately 15° below the horizontal. Additionally, the 3D geometry of this structure appears well represented by an ellipsoid elongated along the quasistreamwise axis running through the center of the structure.

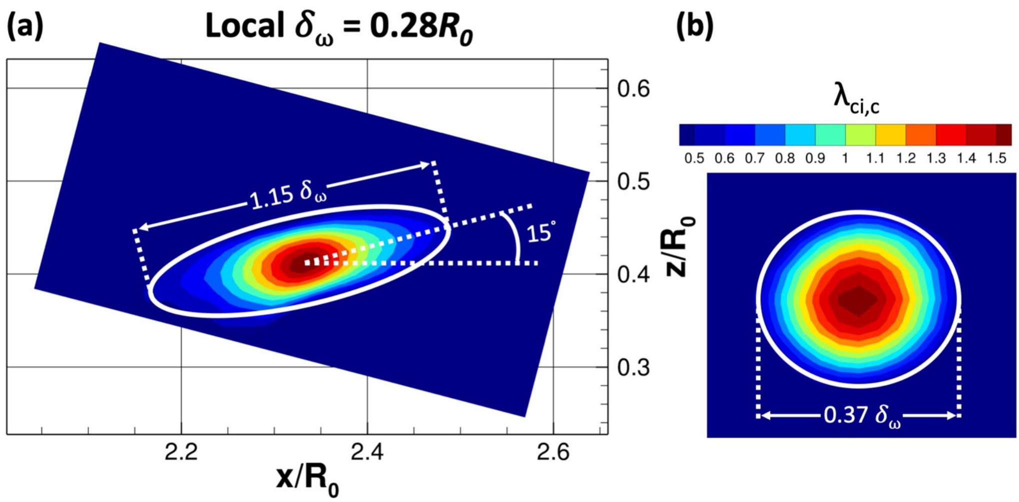

FIG. 10. $\lambda_{ci,c}$ contours from the LSE-resolved flow field in Fig. 9. (a) Cross-sectional plane along $y/R_0 = 0$ and (b) cross-sectional plane viewing along the major axis of the structure [i.e., viewing orthogonally to the dashed black line in Fig. 9(c)].

As mentioned previously, past work by the authors has demonstrated hairpin-shaped vortices to be common turbulent flow features in the shear layer and trailing wake of this flow [26]. Although similar in shape, it is not believed that the quasiaxial structures presented in the current paper are simply representative of the leg segments of these hairpin structures, but that they are in fact a separate type of coherent high-energy turbulent structure existing primarily in the APG regions of this flow. This differentiation of structure type is evidenced by the contrast in both their sizes and angular orientations. For reference, a statistically resolved hairpin vortex structure from the work of Ref. [26], which was resolved using LSE on the condition of $E = \lambda_{ci,\theta} < 0$ within this same flow, is shown in Fig. 11. Both the quasiaxial structure of Fig. 9 and the hairpin structure of Fig. 11 were resolved at locations near one another in the separated shear layer. The statistically resolved hairpin structure is much smaller in size than the statistical quasiaxial structure, and their angular orientations relative to the horizontal axis differ by approximately 15°. Thus, these large-scale quasiaxial vortices appear to be a distinctly separate type of coherent flow structure, which primarily exist within the APG regions of the flow near reattachment, and are consistent with past computational simulations and planar visualization experiments of this flow [1,10].

V. PROPER ORTHOGONAL DECOMPOSITION ANALYSIS

A. Convergence spectra

This section examines the modally decomposed turbulent dynamics of this flow field using proper orthogonal decomposition (POD). In general, this technique behaves as a statistical pattern-recognition algorithm by optimizing an n-dimensional spatial and/or temporal data field for the mean-squared value of a desired variable. As the individual TPIV measurement volumes do not exhibit any temporal correlation between them, the method utilized here is the space-only, so-called snapshot POD method, first proposed by Sirovich [45]. This method treats a set of measurement fields as time-random snapshots of the flow, and decomposes the data into a set of spatially dependent modes, which have been optimally decomposed for the basis of the decomposed variable. For example, the turbulent kinetic energy (TKE) of a flow is directly proportional to the square of the velocity fluctuations, so selecting the square of velocity fluctuations as the subject variable in the POD analysis allows the method to decompose the turbulent dynamics on an optimal TKE basis.

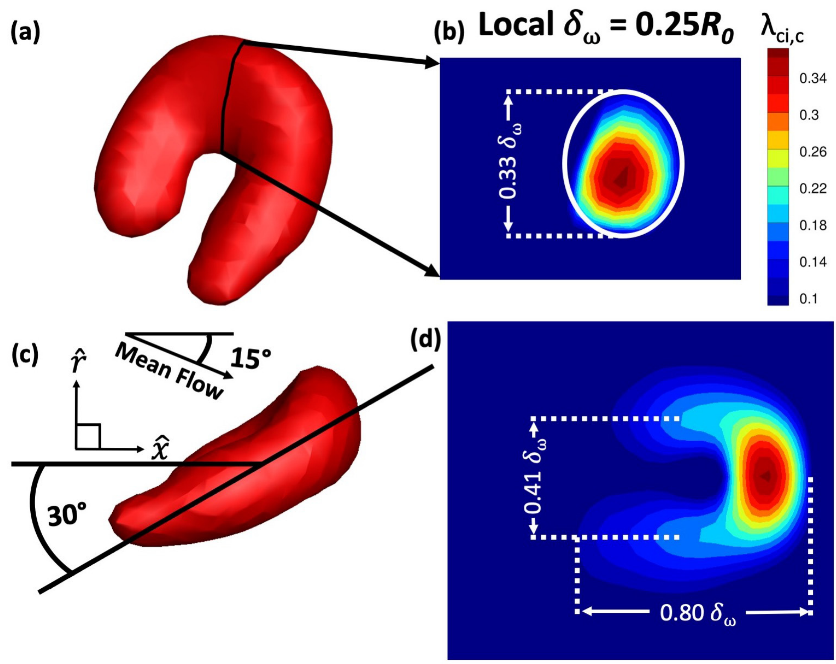

FIG. 11. LSE-resolved hairpin vortex structure within the shear layer of this flow from the previous work of Ref. [26]. (a) 3D view of the structure, (b) cross-sectional slice through the hairpin head, (c) side view of (a) with angular orientation relative to the x axis, and (d) cross-sectional slice through the body of the structure [along the angled black line in (c)]. The structure geometry of (a) and (c) is educed by $\lambda_{\mathrm{ci},c}$, and (b) and (d) are color contoured by $\lambda_{\mathrm{ci},c}$.

Here, the term optimal refers to the method's ability to construct a set of modes that represents the highest fraction of total TKE present in the data in the fewest number of modes possible.

The snapshot POD algorithm and implementation for the current TPIV analysis were inspired by the method of Meyer *et al.* [46]. This same technique was performed in previous work by the authors using SPIV data of this flow field. A detailed stencil outlining the implementation of this method for multidimensional PIV data is given in Ref. [27]. One important aspect of the snapshot POD method is that the fractional TKE represented by each mode can be determined from the relative magnitude of the corresponding eigenvalue for each mode. Thus, the modes can be arranged in descending order of fractional contribution towards the global TKE.

All six TPIV data sets were decomposed on a TKE basis using the square of velocity fluctuations. For reference of the spatial TKE distribution in this flow, a Reynolds-averaged map of TKE [which was measured using SPIV data from Ref. [4], and is defined as $k = 0.5\,\mathrm{tr}(\langle V_i'V_j'\rangle)$] is shown in Fig. 12. The resulting fractional energy spectra from this POD analysis is shown in Fig. 13(a) on a log-log scale. By construction of this method, the snapshot POD algorithm will produce N modes for N input snapshots, where the number of snapshots for each of the six TPIV data sets is listed in Table I. Additionally, the normalized cumulative fractional energy spectra for each of the six data sets are shown in Fig. 13(b) on a semilog scale (i.e., the x axis on this plot is the mode number divided by the total number of modes).

The most significant differences in the POD energy spectra appear in the first few modes. Most notably, the highest energy-containing mode for FOV 3, which measured the recirculation region, accounted for 30% of the local TKE, while all other modes across the six regions had less than 10% fractional TKE each. This relatively low energy fraction in a majority of the modes is unsurprising, however, as the high Reynolds number and Mach number of this flow distribute the turbulent energy

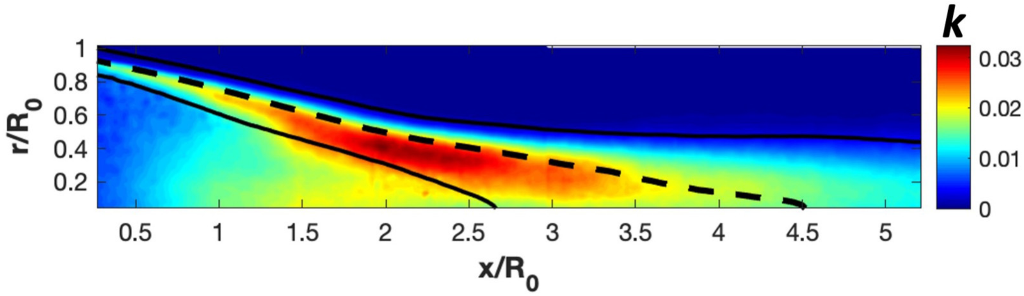

FIG. 12. Turbulent kinetic energy contours from the SPIV data of Ref. [4]. Solid black lines depict the mean shear layer boundaries and the dashed black line depicts the mean sonic line.

across a very broad range of temporal and spatial scales. Between approximately modes 10 and 1000 for each of the six regions, the cumulative energy plots all exhibit a fairly linear decay on the log-log scale, with the slope of this decay approximately equal to -0.93. Table II lists the total number of modes required to achieve both 50% and 90% cumulative TKE for each of the six TPIV data sets, as well as the percentage of modes for each region required to achieve the same benchmarks.

All six TPIV regions required 2.5% or fewer of the total number of modes to achieve 50% energy convergence, with FOV 3 only requiring 0.7% of the modes. In achieving the 90% TKE benchmark, however, the FOV 3 and FOV 4 data sets perform best, requiring just 31.9% and 30.7% of the total number of modes for each region, respectively. For comparison, a similar POD analysis of full field planar SPIV measurements of this flow required 4.3% of the total modes to achieve 50% energy convergence, and 50.9% of the modes to achieve 90% energy convergence [27]. Thus, all six of the TPIV volumetric data sets here were superior in capturing higher energy-containing turbulent motions in a smaller set of modes than the planar SPIV data.

The energy-based decomposition of Fig. 13 only considers the TKE associated with turbulent motions, and has no inherent regard for fluid vorticity. Alternatively, the optimal basis of the decomposition can be changed by changing the input components to the decomposition matrix. For example, the local flow enstrophy (defined as $\varepsilon = |\omega^2|$, where ω is the vorticity vector) represents the strength of local rotational motions within the flow. The input components of the decomposition matrix can be changed from fluctuating velocity components, which gives an

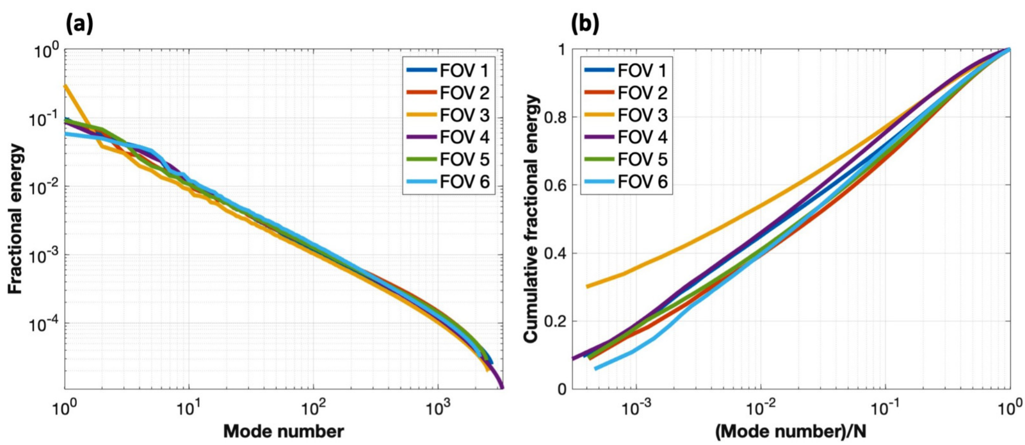

FIG. 13. Energy-based POD: (a) fractional energy versus mode number for all six TPIV fields of view plotted on a log-log scale, and (b) cumulative energy versus mode fraction plotted on a semilog scale.

TABLE II. TPIV POD energy convergence.

Region	No. modes (50% k)	No. modes (90% k)	% modes (50% k)	% modes (90% k)
FOV 1	42	1072	1.6%	39.9%
FOV 2	61	1049	2.5%	43.6%
FOV 3	17	806	0.7%	31.9%
FOV 4	46	1007	1.4%	30.7%
FOV 5	54	1048	2.2%	42.3%
FOV 6	49	870	2.3%	40.1%

energy-based decomposition in the POD analysis, to fluctuating vorticity components (i.e., ω_r', ω_θ', and ω_x' for fluctuating radial, azimuthal, and axial vorticity, respectively), which gives a turbulent enstrophy-based decomposition. Figure 14 displays the convergence spectra for the enstrophy-based decomposition of each of the six TPIV regions, following the same format as Fig. 13.

Comparing Figs. 13 and 14 it can be seen that the convergence rate of the energy-based decomposition across the modes is much faster than that of the enstrophy-based decomposition. The highest enstrophy-containing mode for any of the six TPIV regions only contained 2.4% of the total ε. Similar to Fig. 13(a), Fig. 14(a) displays a nearly linear decay in fractional enstrophy between approximately modes 10 and 500, but here the slopes of decay seem slightly different for each of the six regions. For the cumulative enstrophy convergence [Fig. 14(b)], there appears to be a clear separation of the rates of convergence for the six regions, with FOV 4 (i.e., the reattachment region) having the fastest rate of convergence, and FOV 6 having the slowest. This is consistent with previous results that demonstrated a high prevalence of coherent turbulent motions in the vicinity of shear layer reattachment (FOV 4), and a decay in these coherent motions further downstream (FOV 6). Table III shows the total number of modes and the percentage of modes required to reach both 50% and 90% ε convergence.

From Table III, FOV 4 is clearly the dominant region for fast ε convergence, requiring 6.8% and 41.4% of the total modes to produce 50% and 90% ε convergence, respectively. However, these numbers are in stark contrast to the energy convergence values of Table II, wherein FOV 4 only required 1.4% and 30.7% of the total modes to achieve 50% and 90% TKE convergence, respectively. The differences between the energy-based and enstrophy-based POD analyses can be partly attributed to higher noise levels present in the enstrophy-based analysis, as the fluctuating

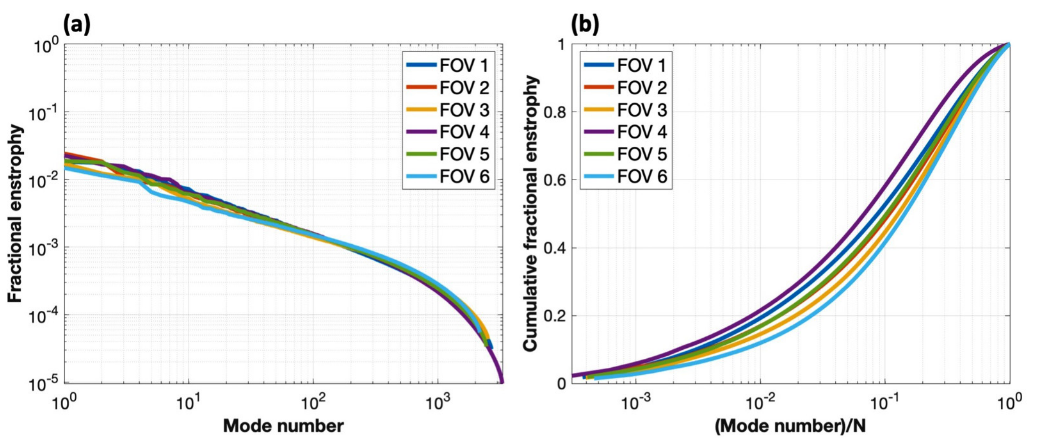

FIG. 14. Enstrophy-based POD: (a) fractional enstrophy versus mode number for all six TPIV fields of view plotted on a log-log scale, and (b) cumulative enstrophy versus mode fraction plotted on a semilog scale.

TABLE III. TPIV POD enstrophy convergence.

Region	No. modes (50% ε)	No. modes (90% ε)	% modes (50% ε)	% modes (90% ε)
FOV 1	235	1420	8.8%	52.9%
FOV 2	260	1349	10.8%	56.0%
FOV 3	322	1488	12.8%	58.9%
FOV 4	224	1359	6.8%	41.4%
FOV 5	252	1332	10.3%	54.4%
FOV 6	312	1322	14.4%	61.0%

vorticity components were computed from spatial derivative quantities, which inherently amplify the noise floor in experimental data. Additionally, it should be noted that for the three TPIV regions that intersected the central axis (i.e., FOV 3, FOV 4, and FOV 6), the enstrophy-based analysis was performed on Cartesian components of the fluctuating vorticity vector to avoid discontinuities in the data along the axis.

B. POD mode shapes

Many of the mode shapes for the TPIV energy-based POD analysis were found to exhibit dynamics that were clearly representative of coherent turbulent structures. In particular, the two highest energy-containing modes for the FOV 1, FOV 2, FOV 4, and FOV 5 data sets (i.e., the two shear layer regions, the reattachment region, and the high-speed trailing wake, respectively) all exhibited dynamics representing either hairpin vortices or the quasiaxial structures of Fig. 10. The FOV 6 energy-based modes, which represent the turbulence in the far central portions of the trailing wake, did not exhibit dynamics that were clearly representative of these types of coherent structures, indicating that the coherent turbulent mechanisms have essentially broken down in this far downstream central flow region. To demonstrate hairpinlike motions within the mode shapes, Fig. 15 displays the first energy-based POD mode from FOV 1, and the second POD mode from FOV 5, displaying both the axial and radial components of the mode, Φ_x and Φ_r, respectively. Additionally, the Φ_θ components for both of the modes in Fig. 15 were found to be near zero.

In Fig. 15, the axial and radial components are oppositely signed relative to one another, which is indicative of directionally consistent velocity fluctuations in the Q2 and Q4 directions, to use the nomenclature of a turbulent quadrant analysis [47] (i.e., a Q2 event has $V_r' > 0$ and $V_x' < 0$ and vice versa for a Q4 event). Note that in Fig. 15 the color scaling is set such that the highest-magnitude contours for both components are depicted in red, and the lowest-magnitude contours are depicted in blue, regardless of sign. In the shear layer [Figs. 15(a) and 15(c)], the highest-magnitude contours of Φ_r and Φ_x exist further downstream, which overlaps spatially with the subsonic high-TKE regions of the shear layer near reattachment (Fig. 12), where previous analyses have demonstrated that the upright and inverted hairpin structures were most prevalent [26]. Just downstream of reattachment [Figs. 15(b) and 15(d)], the high-magnitude Φ_r and Φ_x contours decay with streamwise progression into the trailing wake. This result further emphasizes previously drawn conclusions by the authors that the hairpin structures typically lose energy and coherence the further downstream of reattachment they progress, with a rapid dropoff in these metrics near the end of the APG region. Additionally, various other high-energy modes from the FOV 1, FOV 2, FOV 4, and FOV 5 data sets displayed dynamics similar to Fig. 15 at various spatial frequencies (i.e., having multiple separate regions of paired high-magnitude Φ_r and Φ_x contours within a single mode shape).

An example energy-based mode shape from the FOV 2 region (i.e., the low-speed shear layer) that depicts motions representative of the coherent quasiaxial structures is shown in Fig. 16. Additionally, the amplitude coefficient distribution associated with this mode (which describes how strongly and in what direction a mode is acting during any given snapshot) is shown in Fig. 16(d).

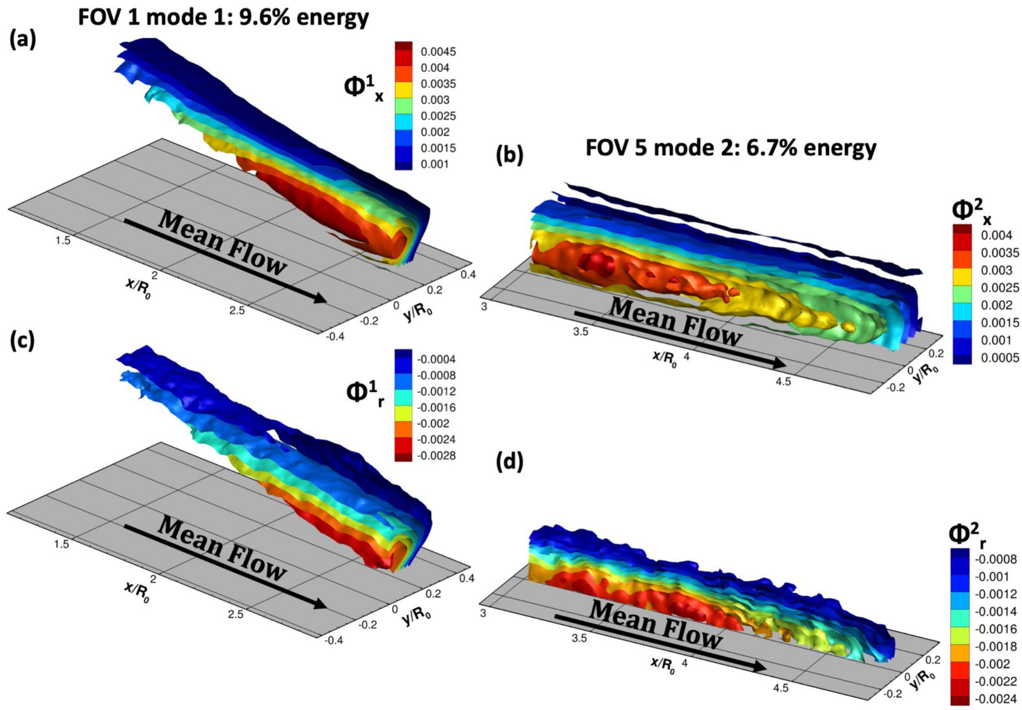

FIG. 15. Isocontours of selected energy-based POD modes from the FOV 1 and FOV 5 data sets projected onto the cylindrical coordinate directions: (a) FOV 1, Φ_x^1; (b) FOV 5, Φ_x^2; (c) FOV 1, Φ_r^1; and (d) FOV 5, Φ_r^2. Note that the coloring for all four figures is such that high-magnitude contours are depicted in red and low-magnitude contours are depicted in blue, regardless of sign.

Note that the color scaling for Fig. 16 is symmetric, such that red contours depict positive values and blue contours depict negative values.

In Fig. 16, all three cylindrical fluctuating velocity components depict oppositely signed high-magnitude regions. This indicates a rotational motion that is both axially rotating (denoted by the alternately signed Φ_r and Φ_θ contours), as well as having a radial component of rotation (denoted by the alternately signed Φ_x contour). However, this 3D rotational motion can be difficult to conceptualize by attempting to visualize the 3D vector field from the corresponding mode components. Alternatively, because the mode components are representative of fluctuating velocity components, they can be treated and analyzed as such. Therefore, computing the vorticity vector on the mode components is physically representative of the vorticity field produced by the turbulent motions depicted by the modes. Figure 17 demonstrates the axial and radial vorticity components for the FOV 2 mode 1 field of Fig. 16.

The 3D isocontours of ω_x and ω_r in Figs. 17(a) and 17(c), respectively, demonstrate a streamwise-elongated region of quasiaxial fluid rotation, centered about the alternately signed regions shown in Fig. 16. However, the cross-sectional slices of ω_x and ω_r in Figs. 17(b) and 17(d), respectively, better demonstrate the conically nested vorticity contours in this region. It was found that the corresponding azimuthal component of vorticity was an order of magnitude smaller than the two components shown in Fig. 17, and was subsequently excluded from this figure. The 2D vorticity contours of Figs. 17(b) and 17(d) closely resemble the intermittency-filtered, ensemble-average contours of axial and radial swirling strength from Fig. 8. The only significant difference between the contours in Figs. 8 and 17 is that for the swirling strength contours, the axial component was notably stronger than the radial component. In Fig. 17, however, both components appear

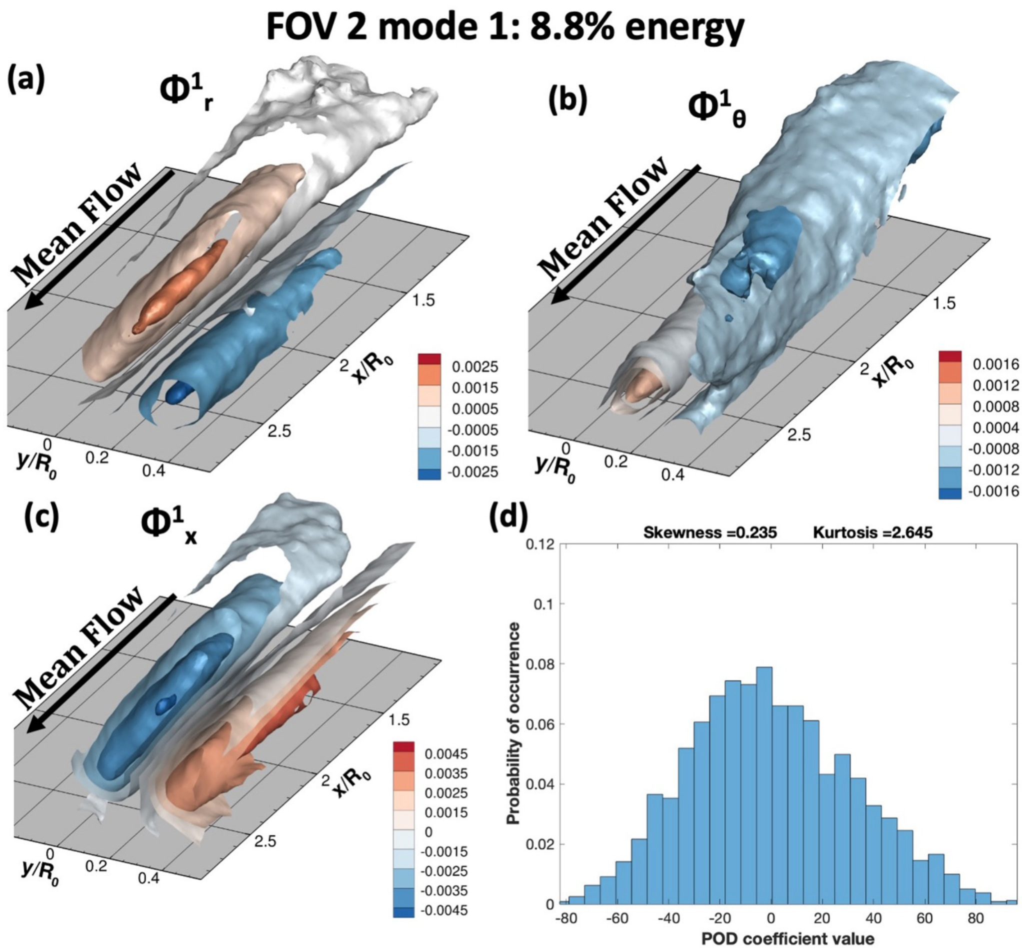

FIG. 16. Isocontours of the FOV 2 energy-based POD mode 1 projected onto the cylindrical coordinate directions: (a) Φ_r^1, (b) Φ_θ^1, (c) Φ_x^1, and (d) corresponding amplitude coefficient distribution.

approximately equal in strength to one another. Nevertheless, these results do seem to indicate that the first energy-based mode of the FOV 2 TPIV data identifies these large-scale quasiaxial coherent structures. Additionally, the amplitude coefficient distribution for this mode [Fig. 16(d)] is quite wide, indicating that these structures can instantaneously exist over a broad range of sizes and energy contributions. Furthermore, similar to the hairpinlike motions of Fig. 15, many other high-energy mode shapes from the FOV 1, FOV 2, FOV 4, and FOV 5 data sets displayed similar motions to Fig. 16 at varying spatial frequencies. This indicates that these types of coherent motion are present across many high-energy modes, and represent a significantly larger fraction of the total TKE than that indicated by just the singular modes in Figs. 15 and 16.

For the enstrophy-based POD analysis, two example mode shapes, one from the FOV 1 data and one from the FOV 5 data, are shown in Fig. 18. Each of the modes shown in Fig. 18 depicts the highest enstrophy-containing mode for that region. Note that, in this figure, each of the components is representative of a corresponding component of fluctuating vorticity, not velocity fluctuations.

It does appear that the two different mode shapes of Fig. 18 depict similar dynamics between the two measurement regions. Both the radial and axial mode components in the two regions depict three alternately signed, streamwise-elongated regions of vorticity. This could be indicative of a

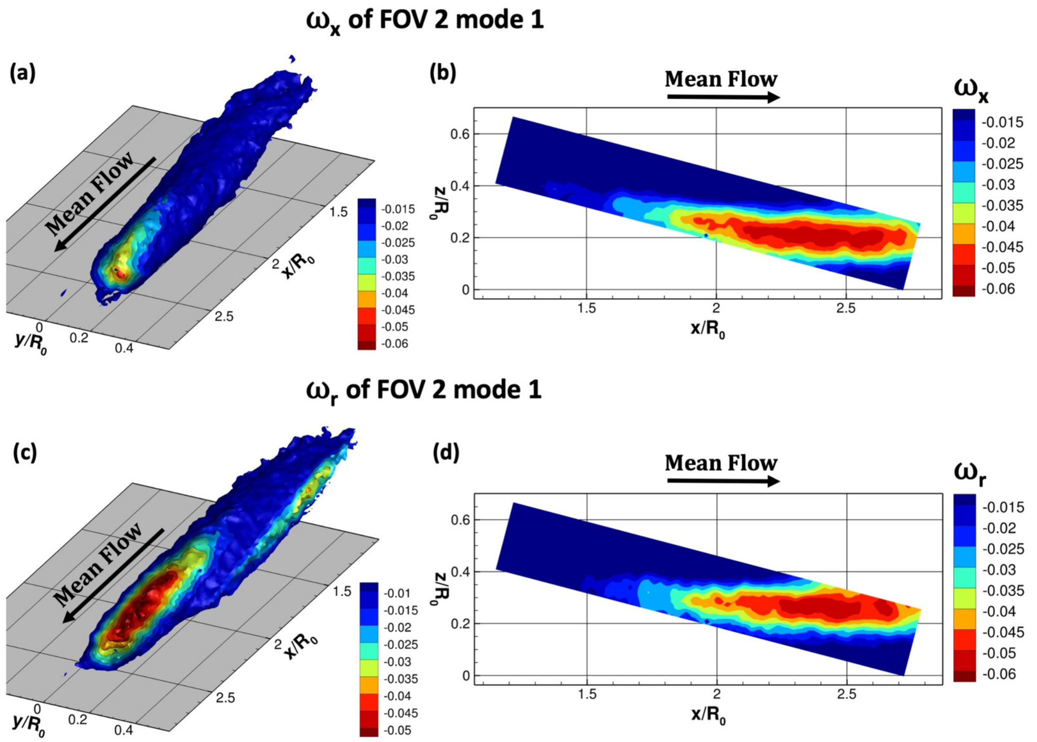

FIG. 17. Components of the vorticity vector computed on the FOV 2 energy-based POD mode 1 vector field: (a) 3D isocontours of ω_x, (b) 2D isocontours of ω_x along the $y/R_0 = 0.2$ plane, (c) 3D isocontours of ω_r, and (d) 2D isocontours of ω_r along the $y/R_0 = 0.2$ plane.

higher spatial frequency correlation of several quasiaxial turbulent structures that exhibit oppositely signed rotation to their neighbor (hence the three alternately signed regions). However, it is unclear if this is the case, as these regions also overlap with regions of non-negligible azimuthal vorticity, which were absent from the quasiaxial structures identified in the energy-based POD analysis in Fig. 17.

C. High-energy motions in the recirculation region

One particular mode from the TPIV energy-based POD analysis distinctly stood out from the others, and that was the highest energy-containing mode from the FOV 3 recirculation region data that contained 30% of the local total TKE. This mode shape is shown in Fig. 19, this time projected onto the Cartesian coordinate directions because of the discontinuities that occur in the mode contour geometries along the $r = 0$ axis. Additionally, the amplitude coefficient distribution for this mode is also shown in Fig. 19(d).

The mode shown in Fig. 19 appears to depict a pulsing motion within the recirculation region, with the strongest motion being in the center of the relatively high-speed portion of the recirculation bubble. Azimuthal motions from this pulsing behavior can be ascertained from the Φ_y and Φ_z contours of Figs. 19(b) and 19(c), but the addition of Φ_x contours of Fig. 19(a) implies that this motion has a helical orientation. The distribution of amplitude coefficients for this mode [Fig. 19(d)] is bimodal, where both peaks occur at a significant distance away from the zero value, and a trough occurs in between the peaks very close to zero. This implies that the motion depicted by this mode is present with significant magnitude in nearly every TPIV snapshot recorded in this region, with

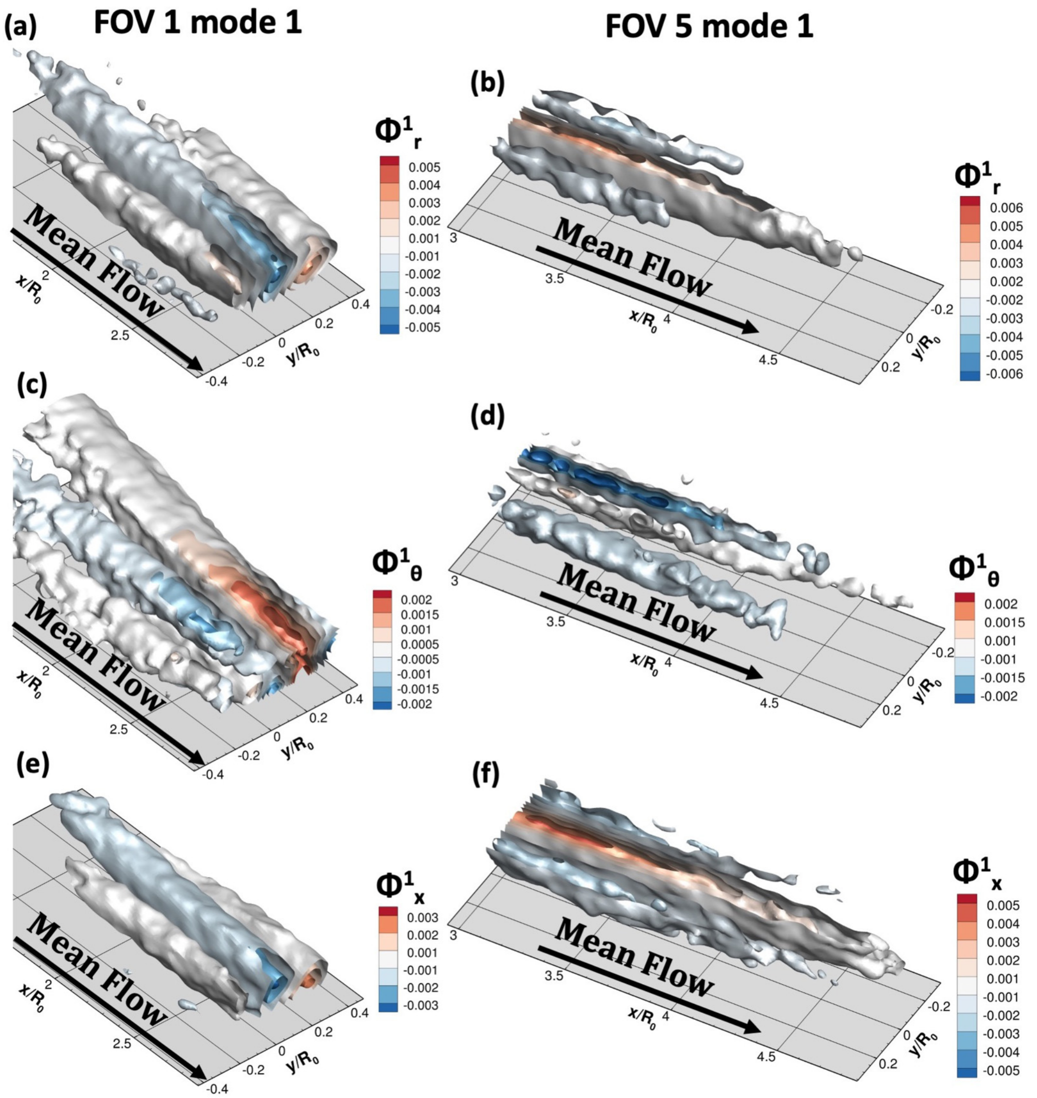

FIG. 18. Projections of selected enstrophy-based POD modes projected onto the cylindrical coordinate directions: (a) FOV 1, Φ_r^1; (b) FOV 5, Φ_r^1; (c) FOV 1, Φ_θ^1; (d) FOV 5, Φ_θ^1; (e) FOV 1, Φ_x^1; and (f) FOV 5, Φ_x^1.

approximately symmetric motions to either side of zero. Additionally, this same type of motion was observed in the highest energy-containing mode from an energy-based POD analysis of the previously mentioned SPIV data of this flow. This first mode from the SPIV POD analysis, which contains 7.5% of the total flow TKE, is shown in Fig. 20 in the same style as Fig. 19. Similar to Fig. 1, the solid black contours in Fig. 20 depict the mean shear layer boundaries, and the dashed black contour depicts the mean sonic line.

The SPIV POD contours from Fig. 20 appear to depict the same motions as the TPIV POD mode from Fig. 19. Additionally, the amplitude coefficient distribution from Fig. 20(d) appears essentially identical to that of Fig. 19(d). Given that the SPIV data were acquired along a flow symmetry plane, the Φ_z (i.e., out-of-plane) contours of Fig. 20(c) directly depict azimuthal motions. This figure implies that there is an alternately signed pulsing motion between the recirculation region

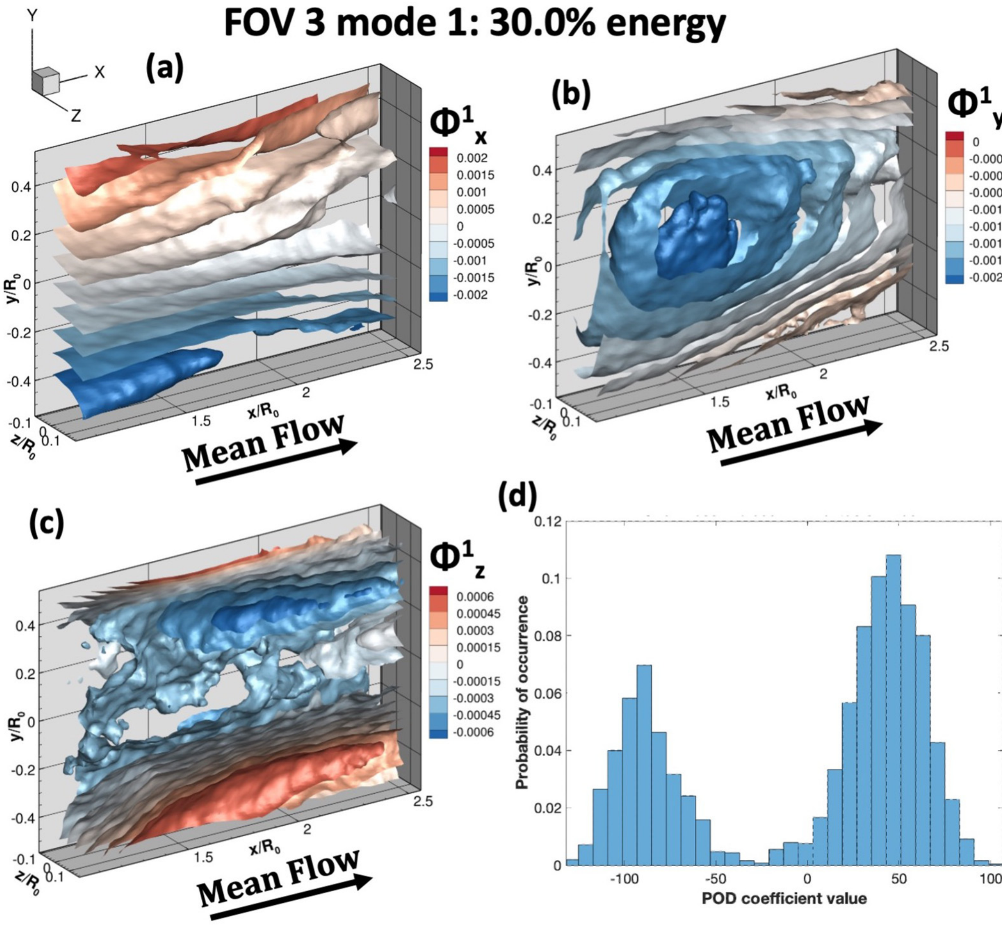

FIG. 19. Isocontours of the first energy-based POD mode from the FOV 3 (recirculation region) data set projected onto the Cartesian coordinate directions: (a) Φ_x^1, (b) Φ_y^1, (c) Φ_z^1, and (d) corresponding amplitude coefficient distribution.

and the low-speed portions of the shear layer. This result could be indicative of a large-scale global flow motion, similar to those identified in compressible planar base flows by Humble *et al.* [48] using snapshot POD. Using time-resolved pressure measurements along the cylinder base of this flow, Janssen and Dutton [24] identified a peak in the power spectral density plots near 850 Hz, which they attributed at the time to some unknown global flow motion related to an interaction between the shear layer and recirculation region. Furthermore, the DNS work by Sandberg [18] found that azimuthal and helical instability modes were dominant within the recirculation region of this flow. The POD analyses for both the current TPIV data and previous SPIV data seem to identify a helically oriented global turbulent motion of the recirculation region and shear layer as the dominant energetic mode shape. This seems to demonstrate a consistency between the current experimental work and the DNS work of Sandberg, even though those simulations were performed at significantly lower Reynolds numbers than the present experimental work. Additionally, Sandberg found that computational elimination of these azimuthal instability modes acted to greatly increase the mean base pressure and reduce pressure fluctuations in these simulations through the reduced production of large-scale structures in the shear layer. However, this was tested experimentally by Reedy *et al.* [49] with the use of triangular splitter plates, which served as the experimental analog to

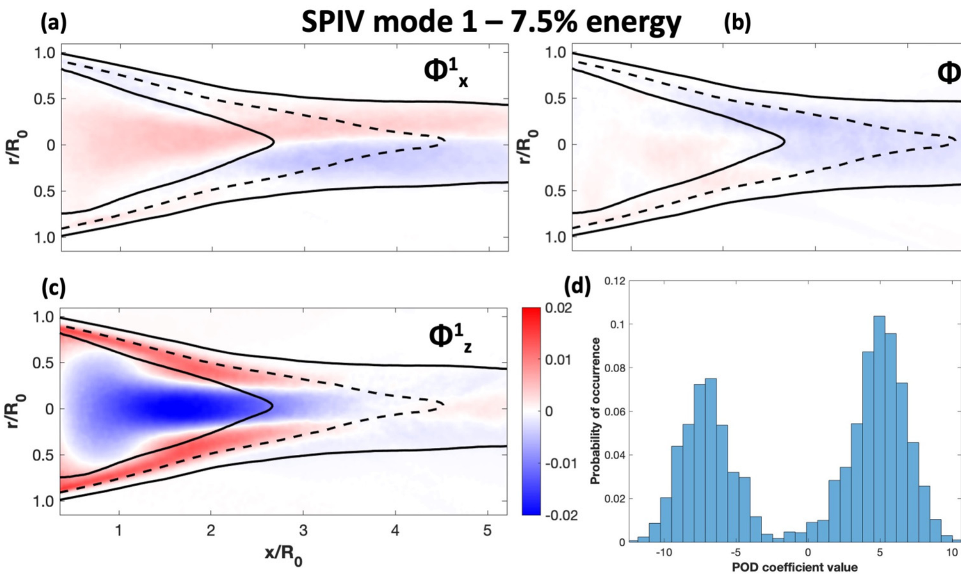

FIG. 20. Contours of the first energy-based POD mode from the planar SPIV POD analysis of Ref. [27]: (a) Φ^1_x, (b) Φ^1_y, (c) Φ^1_z, and (d) corresponding amplitude coefficient distribution.

suppress large-scale azimuthal motions in the recirculation region. In this work it was found that the splitter plates acted to greatly suppress the base pressure fluctuations, but had little to no influence on the time-averaged base pressure. Thus, the true influence of this high-energy helical mode within the recirculation region on the developing properties of this flow remains unclear at this time, but the current experimental work does provide further evidence of its existence.

VI. CONCLUSIONS

The three-dimensional flow structure in a Mach 2.49 longitudinal cylinder wake was investigated experimentally using tomographic particle image velocimetry (TPIV), which measures all three components of velocity throughout a volumetric region. Data were acquired in six different subregions of the flow, including the separated shear layer, the recirculation region, the shear layer reattachment region, and the trailing wake, with a large number of measurement volumes acquired and processed in each region to allow for adequate convergence of statistics in the various analysis methods used.

Large-scale streamwise-elongated structures with a quasiaxial orientation were commonly observed within instantaneous measurement volumes in the regions of the flow encountering the adverse pressure gradient associated with shear layer reattachment. An intermittency-filtered average of two-dimensional swirling strength criteria demonstrated that streamwise-orientated rotations were the dominant component of rotation in the near reattachment region. It was postulated that these motions were generally produced by unsteady components of the instantaneous baroclinic torque in this region of the flow acting as a significant source of vorticity production. Additionally, the statistical geometry and orientation of these quasiaxial structures were demonstrated using linear stochastic estimation. From this analysis, these structures are typically oriented at 15° above the streamwise axis, and are typically longer than one full shear layer thickness.

The snapshot proper orthogonal decomposition (POD) technique was used to decompose the TPIV data into mode shapes. Both energy-based (using fluctuating velocity components) and enstrophy-based (using fluctuating vorticity components) decompositions were performed. The energy-based decomposition was able to represent a significantly higher fraction of turbulent energy within the first few mode shapes than the enstrophy-based decomposition was able to represent the enstrophy. The highest energy-containing mode shapes for four of the six volumetric regions depicted motions representative of coherent turbulent structures. These include upright and inverted hairpin vortices, which were demonstrated in previous work to be highly prevalent structures in this flow, and the previously mentioned quasiaxial structures.

Additionally, the highest energy-containing mode from the recirculation region data depicted large-scale helical motions that represented 30% of the local turbulent energy. These motions were consistent with the highest energy-containing mode from a previous POD analysis of planar stereoscopic PIV data by the authors, and also appear consistent with past direct numerical simulations of this flow. Although these simulations were performed at significantly lower Reynolds numbers than the current experiments, they did predict helical motions in the recirculation region and separated shear layer. These simulations also postulated that low-order azimuthal and helical instability modes in these regions were significant in the generation of large-scale turbulent structures and the production of pressure drag. The current analyses build upon previous works by the authors in the experimental identification and characterization of coherent processes in this highly complex compressible, separated flow, and provide further insights into the dominant turbulent mechanisms.

ACKNOWLEDGMENTS

The authors would like to thank the U.S. Army Research Office for its support of this work with DURIP Equipment Grant No. W911NF-14-1-0404 and Research Grant No. W911NF-15-1-0194. The first author would also like to recognize the financial support provided by the NDSEG fellowship program with sponsorship from the Air Force Office of Scientific Research.

---

[1] F. Simon, S. Deck, P. Guillen, P. Sagaut, and A. Merlen, Numerical simulation of the compressible mixing layer past an axisymmetric trailing edge, J. Fluid Mech. **591**, 215 (2007).

[2] J. L. Herrin and J. C. Dutton, The turbulence structure of a reattaching axisymmetric compressible free shear layer, Phys. Fluids **9**, 3502 (1997).

[3] L. Rollstin, Measurement of inflight base-pressure on an artillery-fired projectile, in *14th Atmospheric Flight Mechanics Conference, Monterey, 1987* (AIAA, Reston, VA, 1987), pp. 195–201.

[4] B. M. Kirchner, J. V. Favale, G. S. Elliott, and J. C. Dutton, Three-component turbulence measurements and analysis of a supersonic, axisymmetric base flow, AIAA J. **57**, 2496 (2019).

[5] J. Gaviglio, J. P. Dussauge, J. F. Debieve, and A. Favre, Behavior of a turbulent flow, strongly out of equilibrium, at supersonic speeds, Phys. Fluids **20**, S179 (1977).

[6] J. L. Herrin and J. C. Dutton, Supersonic near-wake afterbody boattailing effects on axisymmetric bodies, J. Spacecr. Rockets **31**, 1021 (1994).

[7] J. L. Herrin and J. C. Dutton, Supersonic base flow experiments in the near wake of a cylindrical afterbody, AIAA J. **32**, 77 (1994).

[8] J. L. Herrin and J. C. Dutton, Effect of a rapid expansion on the development of compressible free shear layers, Phys. Fluids **7**, 159 (1995).

[9] N. T. Clemens and M. G. Mungal, Large-scale structure and entrainment in the supersonic mixing layer, J. Fluid Mech. **284**, 171 (1995).

[10] C. Bourdon and J. C. Dutton, Planar visualizations of large-scale turbulent structures in axisymmetric supersonic separated flows, Phys. Fluids **11**, 201 (1999).

[11] A. Kastengren, J. C. Dutton, and G. S. Elliott, Large-scale structure visualization and convection velocity in supersonic blunt-base cylinder wakes, Phys. Fluids **19**, 015103 (2007).

[12] A. Kastengren and J. C. Dutton, Large-structure topology in a three-dimensional supersonic base flow, AIAA J. **43**, 1053 (2005).

[13] J. Sahu and C. Nietubicz, Three-dimensional flow calculations for a projectile with standard and dome bases, J. Spacecr. Rockets **31**, 106 (1994).

[14] J. Sahu, Numerical computations of supersonic base flows with special emphasis on turbulence modeling, AIAA J. **32**, 1547 (1994).

[15] J. L. Papp and K. N. Ghia, Application of the RNG turbulence model to the simulation of axisymmetric supersonic separated base flows, in *Aerospace Sciences Meeting and Exhibit, Reno, 2001* (AIAA, Reston, VA, 2001), pp. 1–14.

[16] R. D. Sandberg and H. F. Fasel, Numerical investigation of transitional supersonic axisymmetric wakes, J. Fluid Mech. **563**, 1 (2006).

[17] R. D. Sandberg and H. F. Fasel, Direct numerical simulations of transitional supersonic base flows, AIAA J. **44**, 848 (2006).

[18] R. D. Sandberg, Numerical investigation of turbulent supersonic axisymmetric wakes, J. Fluid Mech. **702**, 488 (2012).

[19] J. Forsythe, K. Hoffmann, R. Cummings, and K. Squires, Detached-eddy simulation with compressibility corrections applied to a supersonic axisymmetric base flow, J. Fluids Eng. **124**, 911 (2002).

[20] R. Baurle, C. Tam, J. Edwards, and H. Hassan, Hybrid simulation approach for cavity flows: Blending, algorithm, and boundary treatment issues, AIAA J. **41**, 1463 (2003).

[21] S. Kawai and K. Fujii, Computational study of a supersonic base flow using hybrid turbulence methodology, AIAA J. **43**, 1265 (2005).

[22] F. Simon, S. Deck, P. Guillen, and P. Sagaut, Reynolds-averaged Navier-Stokes/large-eddy simulations of supersonic base flow, AIAA J. **44**, 2578 (2006).

[23] P. Das and A. De, Numerical investigation of flow structures around a cylindrical afterbody under supersonic conditions, Aerosp. Sci. Technol. **47**, 195 (2015).

[24] J. R. Janssen and J. C. Dutton, Time-series analysis of supersonic base-pressure fluctuations, AIAA J. **42**, 605 (2004).

[25] M. Viji and N. S. Vikramaditya, Modes of base pressure fluctuations: Shape, nature, and origin, AIAA J. **57**, 3933 (2019).

[26] B. M. Kirchner, G. S. Elliott, and J. C. Dutton, Hairpin vortex structures in a supersonic, separated, longitudinal cylinder wake, Phys. Fluids **32**, 046103 (2020).

[27] B. M. Kirchner, G. S. Elliott, and J. C. Dutton, Coherent turbulence and entrainment in a supersonic, axisymmetric, separated/reattaching shear layer, Phys. Rev. Fluids **5**, 084605 (2020).

[28] G. E. Elsinga, F. Scarano, B. Wieneke, and B. W. Van Oudheusden, Tomographic particle image velocimetry, Exp. Fluids **41**, 933 (2006).

[29] M. Samimy and S. K. Lele, Motion of particles with inertia in a compressible free shear layer, Phys. Fluids **3**, 1915 (1991).

[30] C. M. de Silva, R. Baidya, and I. Marusic, Enhancing Tomo-PIV reconstruction quality by reducing ghost particles, Meas. Sci. Technol. **24**, 024010 (2013).

[31] F. Scarano, Tomographic PIV: Principles and practice, Meas. Sci. Technol. **24**, 012001 (2013).

[32] F. Scarano and C. Poelma, Three-dimensional vorticity patterns of cylinder wakes, Exp. Fluids **47**, 69 (2009).

[33] A. Schröder, D. Schanz, B. Heine, and U. Dierksheide, Transitional flow structures downstream of a backward-facing step—an investigation using high resolution tomo PIV, in *Ninth International Symposium on Particle Image Velocimetry, Kobe, Japan, 2011* (unpublished).

[34] B. Wieneke, Volume self-calibration for 3D particle image velocimetry, Exp. Fluids **45**, 549 (2008).

[35] J. Zhou, R. J. Adrian, S. Balachandar, and T. M. Kendall, Mechanisms for generating coherent packets of hairpin vortices in channel flow, J. Fluid Mech. **387**, 353 (1999).

[36] V. Kolar, Compressibility effect in vortex identification, AIAA J. **47**, 473 (2009).

[37] D. Papamoschou and A. Roshko, The compressible turbulent shear layer: An experimental study, J. Fluid Mech. **197**, 453 (1988).

[38] D. A. von Terzi, R. D. Sandberg, and H. F. Fasel, Identification of large coherent structures in supersonic axisymmetric wakes, Comput. Fluids **38**, 1638 (2009).

[39] A. Savitsky and M. J. E. Golay, Smoothing and differentiation of data by simplified least squares procedures, Anal. Chem. **36**, 1627 (1964).

[40] G. E. Elsinga, R. J. Adrian, B. W. Van Oudheusden, and F. Scarano, Three-dimensional vortex organization in a high-Reynolds-number supersonic turbulent boundary layer, J. Fluid Mech. **644**, 35 (2010).
[41] G. L. Brown and A. Roshko, On density effects and large structure in turbulent mixing layers, J. Fluid Mech. **64**, 775 (1974).
[42] F. Stella, N. Mazellier, P. Joseph, and A. Kourta, Scaling of separated shear layers: An investigation of mass entrainment, J. Fluid Mech. **826**, 851 (2017).
[43] R. J. Adrian, B. G. Jones, M. K. Chung, Y. Hassan, C. K. Nithianandan, and A. T. C. Tung, Approximation of turbulent conditional averages by stochastic estimation, Phys. Fluids A **1**, 992 (1989).
[44] K. Christensen and R. Adrian, Statistical evidence of hairpin vortex packets in wall turbulence, J. Fluid Mech. **431**, 433 (2001).
[45] L. Sirovich, Turbulence and the dynamics of coherent structures part 1: Coherent structures, Q. Appl. Math. **45**, 561 (1987).
[46] K. E. Meyer, J. M. Pedersen, and O. Ozcan, A turbulent jet in crossflow analysed with proper orthogonal decomposition, J. Fluid Mech. **583**, 199 (2007).
[47] J. M. Wallace, H. Eckelmann, and R. S. Brodkey, The wall region in turbulent shear flow, J. Fluid Mech. **54**, 39 (1972).
[48] R. Humble, F. Scarano, and B. W. van Oudheusden, Unsteady flow organization of compressible planar base flows, Phys. Fluids **19**, 076101 (2007).
[49] T. M. Reedy, G. S. Elliott, and J. C. Dutton, Passive control of high-speed separated flows using splitter plates, AIAA J. **50**, 1586 (2012).